Cell

Article

Physiological brain clearance architecture revealed by neuronal protein tracing

Graphical abstract

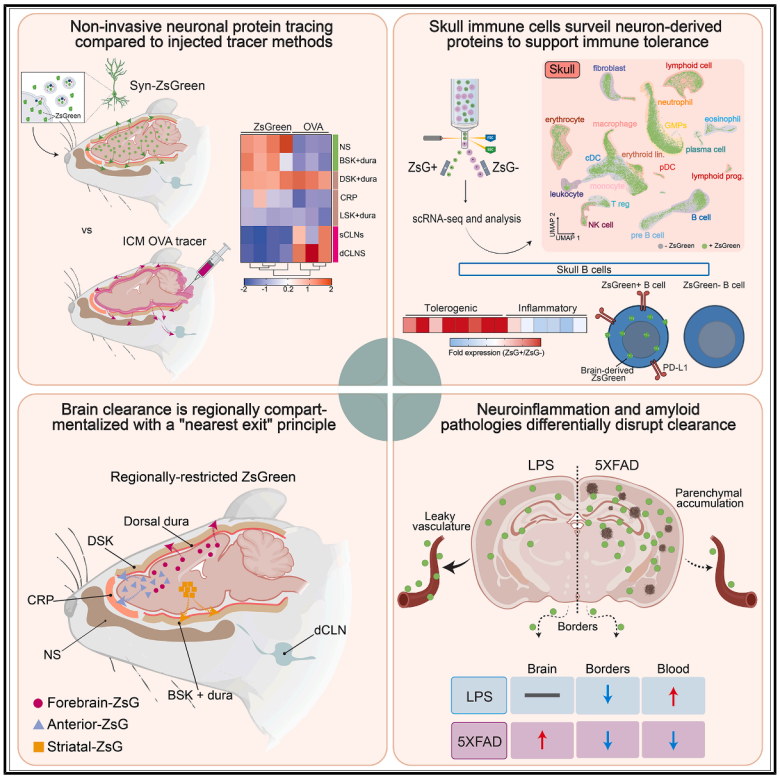

Highlights

- Neuronal protein tracing maps brain border clearance routes distinct from CSF tracers
- Skull borders clear slowly and harbor tolerogenic B cells that sample brain antigens
- Clearance is compartmentalized and follows a "nearest exit" principle by brain region
- Neuroinflammation and amyloid pathology disrupt clearance via distinct mechanisms

Authors

Yuichi Chayama, Nalini R. Rao, Daniela Perla, ..., Zeynep Ilgin Kolabas, Yadong Huang, Andrew C. Yang

Correspondence

andrew.yang@gladstone.ucsf.edu

In brief

Neuronal protein tracing, unlike CSF tracers, reveals that brain clearance follows a "nearest exit" principle through distinct border immune niches disrupted differently by disease.

Chayama et al., 2026, Cell *189*, 1–19
July 23, 2026
https://doi.org/10.1016/j.cell.2026.04.048

CellPress

Please cite this article in press as: Chayama et al., Physiological brain clearance architecture revealed by neuronal protein tracing, Cell (2026), https://doi.org/10.1016/j.cell.2026.04.048

Cell

CellPress
OPEN ACCESS

Article

Physiological brain clearance architecture revealed by neuronal protein tracing

Yuichi Chayama,[1,14] Nalini R. Rao,[1,14] Daniela Perla,[1] Zimo Zhang,[1] Madigan Reid,[1] Sophia Nelson,[1,2] Xinlan Wen,[1] Bella Ding,[1] Jessica Blumenfeld,[1,3] Amanda Apolonio,[1] Sahith Doddipalli,[1] Haoyue Zhou,[1] Sena Gül Turhan,[4] Pu-Yun Shih,[6] Matthias Brendel,[5,7] Ying-Hui Fu,[6,8,9] Ali Ertürk,[4,7,11,12,13] Zeynep Ilgin Kolabas,[4,5,7] Yadong Huang,[1,6] and Andrew C. Yang[1,6,10,15,*]

[1]Gladstone Institute of Neurological Disease, San Francisco, CA, USA
[2]Biomedical Sciences Graduate Program, University of California, San Francisco, San Francisco, CA, USA
[3]Neuroscience Graduate Program, University of California, San Francisco, San Francisco, CA, USA
[4]Institute for Intelligent Biotechnologies, Helmholtz Center Munich, German Research Center for Environmental Health, Neuherberg, Germany
[5]Department of Nuclear Medicine, LMU University Hospital, LMU Munich, Munich, Germany
[6]Department of Neurology, University of California, San Francisco, San Francisco, CA, USA
[7]Munich Cluster for Systems Neurology (SyNergy), Munich, Germany
[8]Weill Institute for Neurosciences, University of California, San Francisco, San Francisco, CA, USA
[9]Kavli Institute for Fundamental Neuroscience, University of California, San Francisco, San Francisco, CA, USA
[10]Bakar Aging Research Institute, University of California, San Francisco, San Francisco, CA, USA
[11]German Research Center for Environmental Health, Neuherberg, Germany
[12]Institute for Stroke and Dementia Research, Klinikum der Universität München, Ludwig-Maximilians-Universität LMU, Munich, Germany
[13]School of Medicine, Koç University, İstanbul, Turkey
[14]These authors contributed equally
[15]Lead contact
*Correspondence: andrew.yang@gladstone.ucsf.edu
https://doi.org/10.1016/j.cell.2026.04.048

SUMMARY

The brain must efficiently clear protein waste to maintain homeostasis, yet physiological drainage pathways remain poorly defined. Standard tracer injection approaches may not reflect endogenous efflux. Here, we develop a non-invasive genetic system to trace neuron-derived protein clearance from the brain to cerebrospinal fluid (CSF) and border tissues. We identify distinct drainage routes and border hotspots missed by tracer injection, confirmed by bioorthogonal labeling of endogenous neuronal proteins. Pulse-chase kinetics reveal slow skull outflow versus rapid dural and nasal clearance. Transcriptomic analyses uncover border cells sampling neuronal antigens, including tolerogenic skull-resident B cells. Region-restricted reporter expression demonstrates compartmentalized clearance following a "nearest exit" principle, where anatomical origin dictates drainage pathway. Disease disrupts clearance through distinct mechanisms: inflammation drives vascular leakage into blood, while amyloid pathology causes parenchymal retention and border exit obstruction. These findings define brain clearance as a compartmentalized system of organized pathways and immune niches whose dysfunction may underlie regional vulnerability in neurological disease.

INTRODUCTION

The brain's high metabolic activity produces waste that must be continuously cleared to maintain neural function and homeostasis.[1–3] In the absence of a conventional lymphatic system, the central nervous system (CNS) relies on a complex network involving cerebrospinal fluid (CSF), perivascular spaces, and meningeal pathways to manage waste clearance.[4–11] CSF, produced primarily by the choroid plexus within the brain's ventricles, bathes the brain and spinal cord and is the conduit for waste clearance via exchange with the brain's interstitial fluid (ISF).[4,12–23] Disruption of brain waste clearance has emerged as a key feature of brain aging and a common hallmark across neurodegenerative diseases, where aberrant accumulation of waste products like amyloid-beta (Aβ) drives cellular dysfunction.[4,24–34] For example, impairments in the glymphatic system,[4,25,33,35–38] which clears waste from the brain via flow-mediated CSF-ISF exchange, have been implicated in Alzheimer's disease (AD).[24,25,27,39–44]

Once waste enters the CSF, its efficient removal relies on an elaborate network of drainage pathways. Over the past decade, tracer injections into the CSF have illuminated the anatomical landscape of viable brain waste clearance pathways and potential exit routes.[4,5,12,15,27,45–54] CSF can drain along perivascular

Please cite this article in press as: Chayama et al., Physiological brain clearance architecture revealed by neuronal protein tracing, Cell (2026), https://doi.org/10.1016/j.cell.2026.04.048

channels before reaching one of several fates: drainage via arachnoid granulations,[5,6,55] cranial nerve sheaths,[15,56] meningeal lymphatics in the dorsal[5,6,27,57,58] or basal[9,54,59] aspects of the dura,[5,9,12] the skull,[60–64] and the cribriform plate[16,19,55,65–70] and nasal cavity[16,19,32,50,59,69,71] en route to the draining cervical lymph nodes.[10,32,54,59,65,72] While these approaches have mapped where CSF and solutes could anatomically flow, the relative utilization of each CNS drainage pathway for the clearance of brain-derived proteins remains an important open question. A significant consideration in interpreting these studies is that pressure-driven tracer infusion can alter intracranial pressure and fluid dynamics, potentially obscuring physiological efflux routes and forcing open anatomical paths, even at low volumes and flow rates.[35,73–77] Furthermore, technical variation in tracer type, doses, volumes, anesthesia, and experimental protocols has led to conflicting results between studies.[18,22,44,78–80] While alternative approaches tracking disease-relevant proteins such as Aβ have provided insight into pathology-specific clearance, the unique disease-predisposing biophysical properties and aggregation-prone nature of these proteins may skew their drainage distribution and sites of accumulation in ways that may not reflect the handling of the broader set of CNS proteins.[4,40,42,44,48]

To complement existing approaches and elucidate the clearance routes of brain-derived proteins from their site of origin, we developed a non-invasive system to genetically express and track a fluorescent reporter secreted from neurons without altering fluid dynamics. This approach was inspired by pioneering studies tracking antigen transfer and immune surveillance in cancer immunology by using the highly stable, soluble, and biologically inert fluorescent protein ZsGreen.[81–85] In adopting this established system for the CNS, we reveal the physiological clearance architecture of neuron-derived proteins. To ensure these findings reflect native protein handling, we validated our reporter using endogenous biorthogonal proteome labeling and compared our results to multiple tracer injection paradigms. Using these techniques, we define the hierarchy of exit routes, identify surveilling immune cells at neuro-immune checkpoints, determine how clearance pathways are regionally organized, and investigate how they are disrupted in models of neuroinflammation and neurodegenerative disease.

RESULTS

A genetic system to trace the clearance of neuron-derived proteins

To identify the physiological routes through which brain-derived proteins exit the CNS, we sought a strategy to express and track the clearance of an endogenously expressed reporter from the brain. To do this, we adapted a Cre-dependent system to drive expression of ZsGreen[81] selectively in neurons. In this paradigm, 2- to 4-month-old ZsGreen reporter mice (ZsG) were intravenously administered AAV-PHP.eB-hSynapsin1-Cre to induce neuron-specific expression and secretion of ZsGreen protein (Syn-ZsG mice) (Figure 1A). Immunostaining, western blot (WB), and fluorescence-based quantification of brain homogenates confirmed robust brain-wide ZsGreen expression in Syn-ZsG mice relative to PBS-injected wild-type (WT) controls 2 weeks after transduction (Figures 1B–1D). To confirm that neuron-derived ZsGreen enters the extracellular space for clearance, we biochemically fractionated[81,86] cortical tissue into extracellular vesicle (EV) and soluble components (Figure S1A). Enrichment of Tsg101 validated the EV enrichment process (Figures S1B and S1C).[87] Critically, ZsGreen was significantly elevated in both the EV and soluble fractions from Syn-ZsG brains, demonstrating that it is actively secreted and available within the brain's ISF for subsequent clearance (Figures 1E and 1F).

To visualize ZsGreen expression in the brain and investigate potential transfer to non-neuronal populations, we performed immunohistochemistry (IHC) on brain sections from Syn-ZsG and WT mice. As expected, ZsGreen colocalized with Cre and the neuronal marker NeuN (Figure 1G). Notably, ZsGreen puncta were also observed in non-neuronal cells lacking Cre expression, including astrocytes (glial fibrillary acidic protein [GFAP$^+$]), vascular endothelial cells (CD31$^+$), and microglia (Iba1$^+$), suggesting transfer of neuronal proteins across CNS cell types (Figures 1G, S1D, and S1E). Flow cytometric analysis confirmed this intercellular transfer, showing that a significant proportion of microglia, astrocytes, brain endothelial cells (BECs), and border-associated macrophages (BAMs) were ZsGreen+ in Syn-ZsG mice compared with WT controls (Figure 1H). This demonstrates that neuron-derived proteins are sampled by a diverse array of cell types within the CNS parenchyma. Finally, to visualize the spatial distribution of ZsGreen at the whole-brain level, we performed light sheet fluorescence microscopy (LSFM) on CUBIC-cleared Syn-ZsG brains (Figure 1I). Using wheat germ agglutinin (WGA-647) and alpha smooth muscle actin (αSMA) to label vasculature, this analysis confirmed broad ZsGreen expression in the brain with notable punctate signal at vascular interfaces (Figure 1J).

Together, these data establish the Syn-ZsG system as a robust platform for tracking the secretion and movement of a neuronal protein from its site of origin. We next used this system to map its precise exit routes from the brain.

Drainage routes for brain-derived proteins differ from CSF-injected tracers

To understand how the clearance of brain-derived proteins compares with conventionally injected tracers, we performed intracisterna magna (ICM) injections of fluorescently labeled ovalbumin (OVA-555 or OVA-647) in Syn-ZsG mice. 1-h post-injection,[4,52,53,59,88] we collected brain border tissues or cleared whole heads for tissue clearing and 3D imaging LSFM analysis to visualize and quantify the distribution of both ZsGreen and OVA across drainage sites within the same mice (Figure 2A). Immunostaining of the brain, dura, nasal cavity, and superficial cervical lymph nodes (sCLNs) was performed to verify that brain border tissues were Cre-negative (Figure S2A). LSFM imaging of the whole mouse head revealed striking bulk differences in the localization of the two fluorescent reporters. ZsGreen signal, in addition to being highly abundant in the brain, was also broadly distributed across brain borders. On the other hand, OVA tracer signal was highly concentrated near the injection site (Figure 2B).

To systematically assess the distribution of each tracer, we quantified ZsGreen and OVA-555 levels across a panel of brain border and drainage tissues using fluorescent plate reader

Please cite this article in press as: Chayama et al., Physiological brain clearance architecture revealed by neuronal protein tracing, Cell (2026), https://doi.org/10.1016/j.cell.2026.04.048

CellPress
OPEN ACCESS

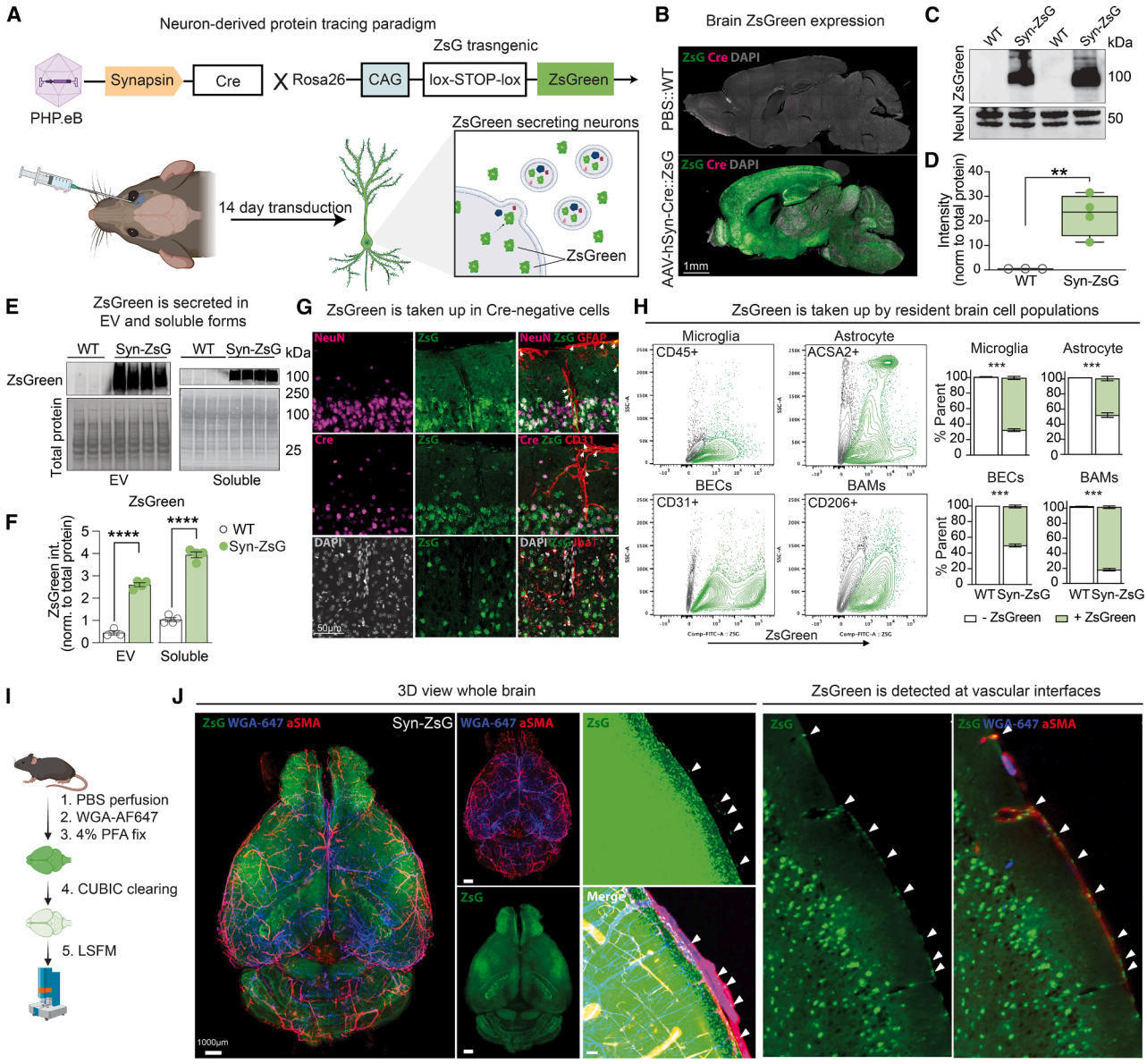

Figure 1. A genetic system to trace the *in vivo* distribution of brain-derived proteins

(A) Schematic of experimental paradigm. ZsGreen reporter expression is induced in neurons via retroorbital delivery of AAV-PHP.eB-hSynapsin1-Cre into ZsGreen-Cre transgenic mice (Syn-ZsG). ZsGreen, produced in neurons, is secreted in soluble form and EVs.

(B) IHC of brain sections confirms neuronal expression of ZsGreen in Syn-ZsG mice compared with PBS-injected WT controls.

(C and D) WB and fluorescent plate reader analysis of brain homogenates verifies significantly increased ZsGreen abundance in Syn-ZsG animals compared with WT controls.

(E and F) Biochemical fractionation of EV and soluble fractions of Syn-ZsG brain homogenates shows ZsGreen is present in both, confirming its secretion. (F) Quantification of WB shows significantly more ZsGreen abundance in Syn-ZsG mice.

(G) IHC reveals ZsGreen (green) within Cre-positive neurons (magenta) and also small puncta within Cre-negative astrocytes (GFAP), vascular endothelial cells (CD31), and microglia (Iba1), suggesting transfer to non-neuronal populations.

(H) Flow cytometry of brain homogenates reveals significant uptake of ZsGreen by astrocytes (ACSA2^{+}), microglia (CD45^{mid}CD11b^{+}), BECs (CD31^{+}), and BAMs (CD206^{+}) in Syn-ZsG. Stars indicate comparisons of ZsGreen+ cells in WT versus Syn-ZsG.

(I) Schematic of the CUBIC clearing of Syn-ZsG brain and 3D imaging LSFM workflow used to assess whole-brain ZsGreen distribution.

(J) LSFM imaging of Syn-ZsG brains reveals widespread ZsGreen distribution, with notable signal localizing at vascular sites labeled by WGA-647 perfusion (pan blood vessels) and αSMA. White arrows indicate ZsGreen at vascular interfaces.

All data are mean ± SEM with n = 3–4. *$p \leq 0.05$, **$p \leq 0.01$, ***$p \leq 0.001$, and ****$p \leq 0.0001$ by Student's t test.

See also Figure S1.

Please cite this article in press as: Chayama et al., Physiological brain clearance architecture revealed by neuronal protein tracing, Cell (2026), https://doi.org/10.1016/j.cell.2026.04.048

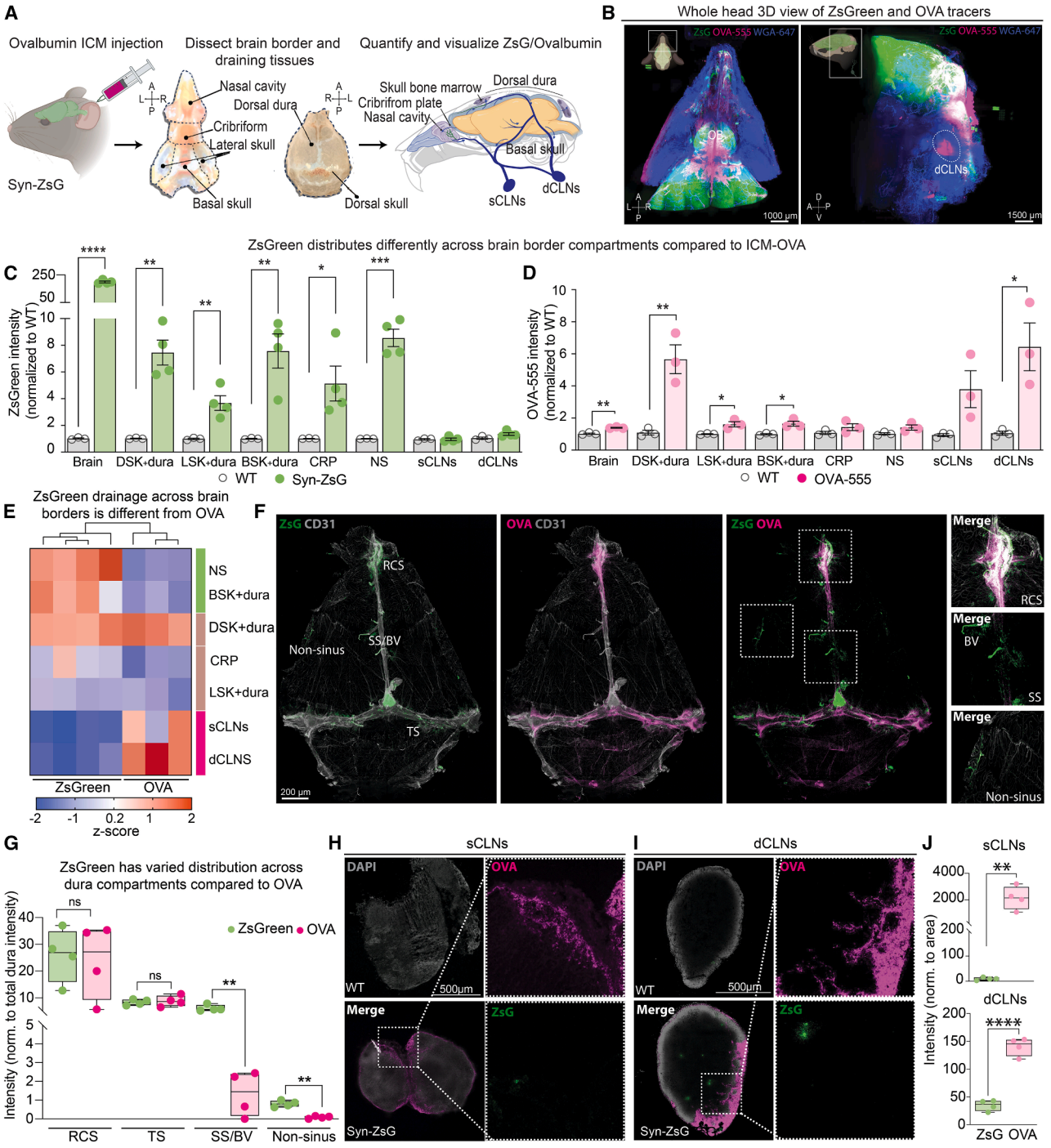

Figure 2. Drainage routes for brain-derived proteins differ from ICM-injected tracers

(A) Schematic of the experimental workflow. For imaging experiments, mice were administered ICM injections of OVA (OVA-647 or OVA-555) to compare exogenous tracer distribution with brain-derived protein efflux (Syn-ZsG). 1-h post-injection, whole heads were fixed and processed for tissue clearing and LSFM. (B) LSFM imaging of whole-head CUBIC-cleared Syn-ZsG mice reveals divergent spatial distribution patterns for neuron-derived ZsGreen and ICM-injected OVA-555. OVA-555 signal is concentrated near the injection site at the base of the brain, whereas ZsGreen signal is highly expressed in the brain and broadly dispersed. (C and D) Quantification of ZsGreen in Syn-ZsG mice (C) and OVA-555 from ICM-injected WT mice (D) intensities across brain borders and drainage tissues using fluorescence plate reader analysis. Fluorescent intensities from bulk homogenates were normalized to total protein and respective WT control tissues to enable comparison across samples of fold changed ZsGreen or OVA-555 abundance. ZsGreen was significantly enriched in the Syn-ZsG dorsal dura and skull (DSK + dura), lateral skull (LSK + dura), basal skull (BSK + dura), cribriform plate (CRP), and nasal cavity (NS), with relatively low levels in sCLNs and dCLNs. By contrast, OVA-555 showed high enrichment in sCLNs and dCLNs.

(legend continued on next page)

Please cite this article in press as: Chayama et al., Physiological brain clearance architecture revealed by neuronal protein tracing, Cell (2026), https://doi.org/10.1016/j.cell.2026.04.048

analyses. Fluorescence signals were normalized to both total protein and respective WT controls to enable direct comparisons between brain borders and tracers (Figures 2C and 2D). As expected, ZsGreen was significantly enriched in the brain of Syn-ZsG mice (Figure 2C). Compared with WT controls, the ZsGreen signal was significantly elevated across nearly all tissues examined, with significant enrichment in the dorsal, lateral, and basal skull + respective dura, nasal cavity, and cribriform plate. Notably, however, the sCLNs and deep cervical lymph nodes (dCLNs) showed minimal ZsGreen. By contrast, OVA displayed a markedly different distribution profile. ICM-injected OVA levels were lower in the nasal cavity and cribriform plate but were found significantly higher in the sCLNs and dCLNs, demonstrating rapid efflux to collecting lymph nodes, likely bypassing the brain[47] (Figure 2D). A heatmap of *Z* scored fluorescence intensities (from Figures 2C and 2D) across border tissues and lymph nodes revealed three major clusters. A heatmap of *Z* scored fluorescence intensities (from Figures 2C and 2D) revealed three clusters: tissues enriched for ZsGreen (nasal cavity, basal skull + dura), tissues with similar ZsGreen and OVA (dorsal/lateral skull + dura, cribriform plate), and tissues preferentially enriched for OVA (cervical lymph nodes) (Figure 2E). These results demonstrate that brain-derived proteins distribute differently and likely exit through routes distinct from those used by injected tracers.

Interestingly, even in tissues where both tracers were present at similar overall levels, such as the dorsal dura, we observed different within-tissue distributions comparing ZsGreen and OVA. In dural whole mounts from Syn-ZsG mice, ZsGreen and OVA both colocalized with $CD31^+$ vasculature (perisinusal localization), but only ~40% of ZsGreen signal overlapped with OVA, suggesting distinct uptake or accumulation sites within the dura (Figure S2B). ZsGreen accumulated at specific sinus structures, especially the bridging veins of the sagittal sinus (SS), likely reflecting drainage through recently discovered arachnoid cuff exit (ACE) points,[89] as well as in non-sinus regions of the dura (Figures 2F and 2G). Immunostaining of sCLNs and dCLNs confirmed significant OVA accumulation and relatively sparse ZsGreen signal (Figures 2H–2J and S2C). Together, these data suggest that the drainage routes of brain-derived proteins differ from those of injected tracers.

To verify that our ZsGreen paradigm reflects the drainage of endogenously produced neuronal proteins rather than an artifact of the reporter itself, we leveraged an *in vivo* bioorthogonal proteome-labeling system (PheRS).[90] In this system, Cre-dependent incorporation of a blood-brain barrier (BBB)-permeable, non-canonical amino acid (AzF), administered intraperitoneally (i.p.), occurs into all newly synthesized proteins. Using the same Syn-Cre AAV strategy, neuronal proteins incorporate AzF, rendering them click-detectable (Syn-PheRS). Following 1 week of AzF administration, immunostaining and in-gel fluorescence analyses confirmed AzF-labeled neuronal proteins (AzF-647) in Syn-PheRS mice compared with controls (Figures S2D–S2F). Consistent with our ZsGreen findings, immunostaining and in-gel fluorescence analyses from Syn-PheRS mice demonstrated that endogenous neuronal proteins mirror the anatomical distribution of ZsGreen in dura and are present at brain borders (Figures S2G–S2K). Together, these data validate ZsGreen as a faithful reporter of the drainage of endogenous neuronal proteins.

A critical question is whether the divergent distributions of ZsGreen and ICM-injected OVA was due to the site of origin (parenchyma versus CSF) or tracer duration (chronic versus acute), as ZsGreen accumulates over a 2-week transduction period while OVA is assessed 1 h after injection. To address this, we chronically administered OVA into the CSF using an osmotic pump for 2 weeks (matching the ZsGreen production window) and quantified its distribution across brain-border tissues and draining lymph nodes. Chronically delivered OVA exhibited a distribution pattern similar to acute ICM-injection, including comparable representation in the dura, underrepresentation at skull-associated borders, and significant enrichment in both sCLNs and dCLNs (Figures S2L and S2M). These findings demonstrate that the distinct drainage routes observed for brain-derived proteins versus injected tracers are not attributable simply to differences in tracer duration.

Brain-derived proteins exit the CNS through distinct anatomical compartments with border-specific clearance kinetics

To visualize the global distribution of brain-derived proteins as they exit the CNS, we performed 3D LSFM on whole, CUBIC-cleared heads from Syn-ZsG mice after ICM injection of OVA-555 tracer, revealing an unexpected ZsGreen clearance route extending laterally along the zygomatic process that was not highlighted by OVA-555 (Figures 3A and 3B). In the nasal cavity, ZsGreen concentrated above the dorsal medial meatus (DMM) and along lateral nasal glands (LNGs), with IHC confirming

(E) Data from (C) and (D) plotted as a heatmap of *Z* scored fluorescence intensities across tissues highlights three distinct drainage profiles: tissues with comparable signals for both tracers (brown), tissues with preferential OVA accumulation (pink), and tissues with elevated ZsGreen signal (green), indicating distinct clearance routes for endogenous proteins versus exogenous tracer.

(F) IHC of dura whole mounts demonstrates both ZsGreen and OVA signal localize along the $CD31^+$ dural sinuses, with notable enrichment in the SS/BV and rostral confluence of sinuses (RCS).

(G) Regional anatomical analysis of tracer distribution within dura. Fluorescence intensity of ZsGreen and OVA was measured at major sinus regions (RCS, TS, SS/BV) and in non-sinus areas, then normalized to total tracer intensity across the dura.

(H and I) Representative IHC images of sCLNs and dCLNs from WT and Syn-ZsG mice. OVA signal is prominent in both lymph nodes, while ZsGreen signal is comparatively low.

(J) Quantification of fluorescence intensities from (H) and (I), normalized to tissue area. ICM-injected OVA signal is significantly higher than neuron-derived ZsGreen in both sCLNs and dCLNs. SS/BV, sagittal sinus/bridging veins; RCS, rostral confluence of sinus; TS, transverse sinus; DSK, dorsal skull; LSK, lateral skull; BSK, basal skull; CRP, cribriform plate; NS, nasal cavity; sCLNs and dCLNs, superficial and deep cervical lymph nodes. All data are mean ± SEM with $n = 3$–4. $^*p \leq 0.05$, $^{**}p \leq 0.01$, $^{***}p \leq 0.001$, and $^{****}p \leq 0.0001$ by one-way ANOVA with Tukey's post hoc or Student's *t* test.

See also Figure S2.

Please cite this article in press as: Chayama et al., Physiological brain clearance architecture revealed by neuronal protein tracing, Cell (2026), https://doi.org/10.1016/j.cell.2026.04.048

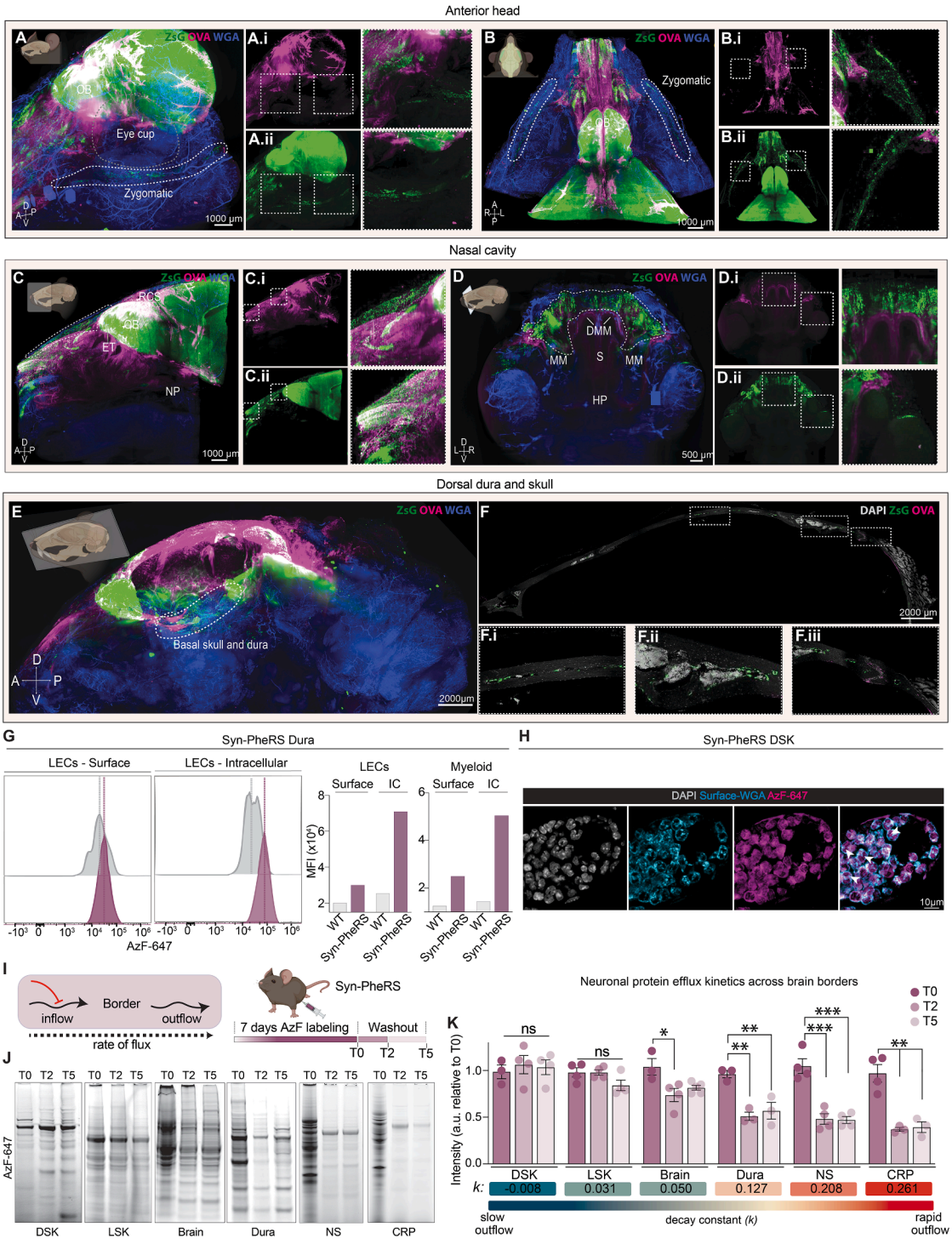

Figure 3. Distinct drainage hotspots and clearance kinetics for brain-derived proteins

(A and B) LSFM of CUBIC-cleared whole anterior heads from Syn-ZsG mice following ICM injection of OVA-555. LSFM imaging reveals a prominent ZsGreen clearance route extending laterally along the zygomatic process that is not shown by OVA (magenta), indicating selective efflux of brain-derived proteins through bone-associated pathways. (i and ii) Merged channels.

(C and D) LSFM imaging of the NS identifies additional routes of ZsGreen exit. Sagittal (C) and coronal (D) views show ZsGreen concentrated in discrete hotspots above the DMM and along LNGs, as well as within naso- and ethmoturbinates, with a distribution distinct from OVA. (i and ii) Insets highlight regional differences in ZsGreen and OVA localization.

(E) LSFM imaging of CUBIC-cleared heads with the brain removed reveals differential distribution of ZsGreen and OVA across skull and dura compartments. ZsGreen accumulates prominently along dorsal, lateral, and BSK-associated regions, whereas OVA shows limited representation in these compartments.

(legend continued on next page)

Please cite this article in press as: Chayama et al., Physiological brain clearance architecture revealed by neuronal protein tracing, Cell (2026), https://doi.org/10.1016/j.cell.2026.04.048

distributions distinct from OVA (Figures 3C, 3D, and S3A–S3D). This highly structured localization suggests significant efflux of brain-derived proteins to specific functional zones in the anterior head and nasal cavity.

To better resolve tracer distribution in the skull, we removed the brain prior to clearing and LSFM. This revealed marked differences between ZsGreen and OVA-555 across bone-associated structures, including distinct ZsGreen accumulation in the basal and lateral skull regions (Figures 3E, S3E, and S3F). IHC analysis of dorsal skull sections revealed distinct ZsGreen signal within skull bone marrow hubs compared with OVA (Figure 3F). These imaging data demonstrate that brain-derived proteins drain to anatomical compartments at levels underreported by injected tracers.

To determine whether brain-derived proteins are internalized by resident cells at brain borders, we leveraged the Syn-PheRS platform to click-tag endogenously produced neuronal proteins. Flow cytometric analysis of dural cells comparing AzF-647 signal before and after permeabilization revealed that a substantial fraction of AzF-labeled neuronal proteins localized intracellularly within both lymphatic endothelial cells (LECs) and myeloid cells (Figures 3G and S3G). Immunostaining of cleared whole heads and dorsal skull sections followed by click detection and surface labeling confirmed intracellular accumulation of brain-derived proteins within resident cells (Figures 3H, S3H, and S3I; Video S1).

To assess flux dynamics, we performed a Syn-PheRS pulse-chase where, after 7 days of labeling, AzF was withdrawn for 0, 2, or 5 days (Figure 3I). In-gel AzF-647 fluorescence analyses across border tissue homogenates revealed distinct clearance (sum of efflux and degradation) kinetics across compartments (Figures 3J and 3K). Skull-associated borders exhibited slow outflow ($k = -0.008$), whereas the dura, nasal cavity, and cribriform plate showed rapid clearance ($k = 0.127$–0.261). Together, these data demonstrate that brain-derived proteins are actively taken up by resident border cells and that borders exhibit divergent clearance kinetics with slow skull retention versus rapid dural and nasal turnover.

Distinct brain border and skull immune cells surveil brain-derived proteins to support immune tolerance

Having identified key anatomical border sites for drainage, we next sought to define the specific cell types within them that uptake and surveil neuronal proteins. We collected the dorsal dura, dorsal skull, and nasal cavity from Syn-ZsG mice and WT controls. Tissues were dissociated, and ZsGreen+ and ZsGreen− cells were quantified by flow cytometry, then sorted for single-cell RNA sequencing (scRNA-seq) (Figure 4A).

Flow cytometry quantified the proportion of ZsGreen+ and ZsGreen− cells in each tissue. We observed significantly greater ZsGreen sampling by dural cells compared with skull and nasal across cell types such as BECs and conventional dendritic cells (cDC1 and cDC2) (Figures 4B and S4A). In the dorsal dura, for example, approximately 60% of CD206$^+$ BAMs and 65% of BECs were ZsGreen+ compared with ∼35% and ∼15% in skull and nasal tissue, respectively (Figure 4C). IHC analyses corroborated significant uptake of ZsGreen across CD206$^+$ cells at dural sinuses (Figures 4D and S4B). Despite similar bulk ZsGreen levels in dorsal dura and skull versus nasal tissue (Figure 2), brain-derived antigen sampling varied across borders and did not scale with total uptake, suggesting border-specific structural or cellular specialization. To assess transcriptional signatures linked to antigen sampling, we performed scRNA-seq on near-equal numbers of ZsGreen+ and ZsGreen− cells from dura, skull, and nasal cavity. Uniform manifold approximation and projection (UMAP) embedding revealed a complex community of immune, endothelial, and stromal cells at each border[57,62,76,91–93] (Figures 4E–4G and S5A–S5C; Tables S1 and S2). Across all three borders, ZsGreen and Cre transcripts were largely undetectable, indicating ZsGreen+ cells reflect uptake rather than expression (Figures S5D and S5E).

To further investigate cell populations exhibiting distinct transcriptional profiles linked to brain-derived protein uptake, we assessed transcriptional signatures associated with ZsGreen uptake (Figures 4H–4J). As expected, cell types like macrophages exhibited significant ZsGreen uptake across borders. Yet, comparison of ZsGreen+ versus ZsGreen− macrophages revealed minimal transcriptional differences (Figures S5F and S5G; Tables S3, S4, and S5). This implies that macrophage antigen sampling is governed less by specialized transcriptional programs and more by extrinsic factors such as the anatomy of each border and their positioning relative to outflow pathways. Among endothelial and immune populations identified across brain borders, dorsal dura endothelial cells and skull-resident B cells exhibited distinctive transcriptional profiles linked to

(F) Sagittal IHC sections of the DSK demonstrate ZsGreen localization within skull bone marrow hubs compared with OVA, indicating differential access of brain-derived proteins to skull-associated cellular niches. (i–iii) Insets show zoom in of boxed regions.

(G) Flow cytometric analysis of dural cell populations from Syn-PheRS mice following click labeling of AzF-incorporated neuronal proteins (AzF-647). The AzF-647 signal was quantified before and after permeabilization to distinguish surface-associated and intracellular pools, revealing a substantial intracellular accumulation in both LECs and myeloid cells. Bar plots show mean fluorescence intensity (MFI) relative to controls. LECs gated on (CD45$^-$CD31$^+$PDPLN$^+$); myeloid gated on (CD45hiCD11b$^+$). $n = 2$ pooled mice.

(H) Immunostaining of DSK sections from Syn-PheRS mice following click detection of AzF-647. Co-staining with a surface marker (WGA) highlights intracellular localization of neuron-derived proteins within resident skull cells.

(I) Schematic of the Syn-PheRS pulse-chase paradigm used to assess protein flux dynamics across brain borders. After 7 days of AzF labeling, AzF was withdrawn and allowed to wash out for 0, 2, or 5 days.

(J and K) In-gel fluorescence analysis of AzF-647 labeled proteins across brain border tissues reveals compartment-specific clearance kinetics. AzF-647 intensities were normalized to total protein and scaled with respect to T0. Decay constants (k) for each border show that skull-associated borders exhibit slow outflow, whereas the dura, NS, and CRP display faster clearance rates.

All data are mean ± SEM with $n = 3$–5. *$p \leq 0.05$, **$p \leq 0.01$, ***$p \leq 0.001$, and ****$p \leq 0.0001$ by one-way ANOVA with Tukey's post hoc.

See also Figure S3.

Please cite this article in press as: Chayama et al., Physiological brain clearance architecture revealed by neuronal protein tracing, Cell (2026), https://doi.org/10.1016/j.cell.2026.04.048

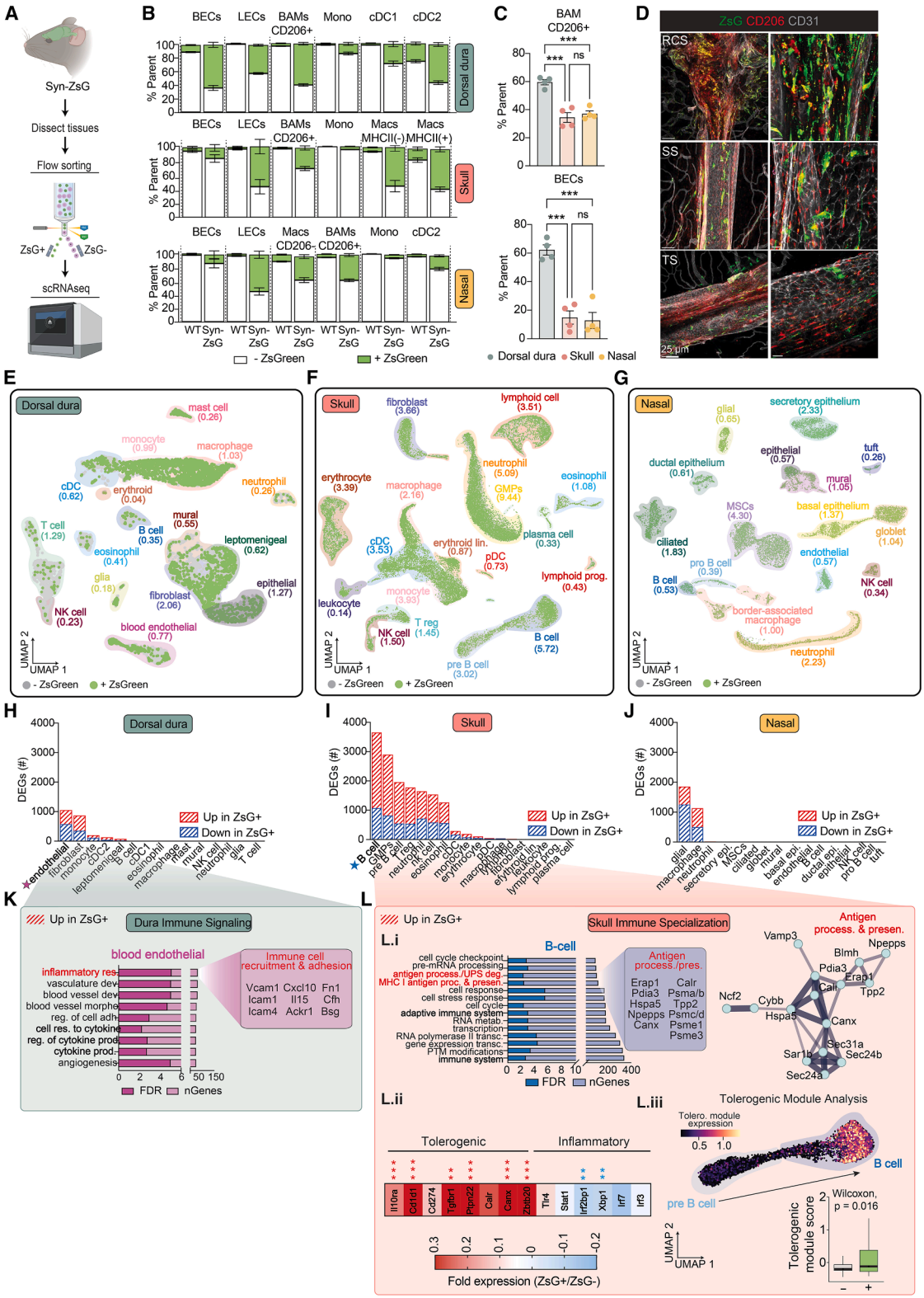

(legend on next page)

Please cite this article in press as: Chayama et al., Physiological brain clearance architecture revealed by neuronal protein tracing, Cell (2026), https://doi.org/10.1016/j.cell.2026.04.048

neuronal protein uptake. Differentially expressed gene (DEG) analysis revealed upregulated genes in ZsGreen+ cells from dorsal dura BECs, which were significantly enriched in pathways associated with immune cell adhesion and recruitment, including key genes such as *Vcam1*, *Icam1*, *Cxcl10*, *Il15*, and *Plcg2* (Figure 4K; Table S3). These results suggest that select dural endothelial cells actively surveil brain-derived antigens and facilitate local immune responses.[57,94]

Notably, skull-resident B cells demonstrated the most pronounced distinct transcriptional profile linked to ZsGreen uptake (Figure 4I; Table S4). ZsGreen+ skull B cells upregulated genes that were enriched for pathways involved in antigen processing and presentation, proteasomal degradation, and vesicular trafficking (Figure 4Li). Core genes involved in antigen processing (*Erap1*, *Pdia3*, *Calr*, *Canx*, and *Hspa5*) were significantly upregulated, along with vesicle trafficking genes such as *Vamp3*, *Sar1b*, and *Sec24a/b* (Figure 4Lii). Concurrently, ZsGreen+ compared with ZsGreen− skull B cells significantly upregulated numerous key tolerogenic markers, including *Il10ra*, *Cd1d1*, *Zbtb20*, and *Ptpn22*, which are involved in limiting immune responses and promoting immune regulation.[63,64,95–97] To confirm this transcriptomic signature at the protein level, we performed quantitative immunostaining for the checkpoint molecule PD-L1 (CD274). We found that ZsGreen+ skull B cells displayed significantly higher PD-L1 protein levels compared with their ZsGreen− counterparts (Figures S5H and S5I). By contrast, classical pro-inflammatory genes such as *Tnf*, *Il1b*, and type I interferon signaling components (*Irf1*, *Irf3*, and *Irf7*) were either unchanged or significantly downregulated (Figure 4Liii). Trajectory analysis revealed a gradual enrichment of tolerogenic module genes (*Ptpn22*, *Zbtb20*, and *Cd274*)[97] from pre-B to B cells (Figure 4Liv). Strikingly, from this analysis, ZsGreen+ cells displayed significantly higher tolerogenic module expression compared with ZsGreen−. Expanding on and consistent with prior studies,[63,64,95,96] these data suggest that a distinct population of skull B cells take up and drive a tolerogenic immune response to brain-derived antigens.

Brain regions preferentially utilize nearby drainage routes to clear neuron-derived proteins

Having established the overall architecture of brain-wide neuronal protein clearance, we next asked whether this system is uniform or spatially compartmentalized (Figure 5A). We asked whether proteins from distinct brain regions drain via common or unique pathways by restricting Cre-mediated ZsGreen production to select brain regions and comparing ZsGreen clearance dynamics. Compared with our pan-neuronal Syn-ZsG model, we generated three regionally restricted ZsG models: (1) forebrain-ZsG (CaMKII-Cre) labeling forebrain excitatory neurons; (2) anterior-ZsG (AAV:hDLX-4X2C-Cre)[98] labeling forebrain and olfactory bulb GABAergic interneurons; and (3) striatal-ZsG (AAV:AiE0441h_3xC2-Cre)[99] labeling striatal medium spiny neurons. We confirmed successful, region-specific ZsGreen expression in each paradigm (Figure 5B).

As total brain ZsGreen levels varied across paradigms, we normalized all border tissues by total brain ZsGreen and quantified the relative utilization of each border (Figure 5C). Comparison of relative border utilization revealed a divergence in the drainage pathways engaged by each brain region (Figures 5D and S6A). Across all three regionally restricted models, the ZsGreen signal was enriched at borders proximal to the labeled region and reduced at distal borders (Figure 5E). For example, dorsal dura exhibited significantly greater ZsGreen drainage in forebrain-ZsG mice compared with striatal-ZsG mice. Conversely, the nasal cavity showed significantly greater

Figure 4. Distinct brain border and skull immune cells surveil brain-derived proteins to support immune tolerance

(A) Schematic of the experimental workflow. Dorsal dura, DSK, and NS tissues were collected from Syn-ZsG and WT mice. Isolated endothelial, stromal, and immune cell types were analyzed by flow cytometry to quantify relative levels of ZsGreen uptake. Cells of each types major cell type were then sorted into equal proportions of ZsGreen+ and − cells for scRNA-seq.

(B) Flow cytometry-based quantification of the proportion of ZsGreen+ and − cells within each immune cell population in the dorsal dura, skull, and nasal, based on flow cytometry. BECs: CD45(−)CD31+; LECs: CD45(−)CD31(−)PDPLN+; cDC1: CD45hiCD11b(−)CD11c+; cDC2: CD45hiCD11b+CD11c+MHC II+; CD206+ BAMs: CD45hiCD11b+CD206+; monocytes: CD45hiCD11b+Ly6C+; macrophages: CD45hiCD11b+F480+CD206(−).

(C) Comparison of ZsGreen+ populations of CD206$^+$ BAMs and CD31$^+$ BECs across brain border tissues shows that dural resident cells take up significantly more ZsGreen compared with cells residing in both skull and nasal compartments.

(D) Immunofluorescence of dorsal dura whole mounts from Syn-ZsG mice reveals colocalization of ZsGreen with CD206$^+$ BAMs and CD31$^+$ vasculature. The ZsGreen signal shows perisinusal accumulation, including the RCS, SS, and TS.

(E–G) UMAP projections of scRNA-seq data from dorsal dura (E), skull (F), and NS (G), background shaded color for each cluster represents annotated cell type. Green dots represent ZsGreen+ cells, gray dots represent ZsGreen− cells.

(H–J) Bar plots summarizing the number of DEGs between ZsGreen+ and ZsGreen− cells by cell type in dorsal dura (H), skull (I), and NS (J). The skull shows substantially greater transcriptional differences in ZsGreen+ versus ZsGreen− immune cells, compared with similar populations in the dura and nasal tissue.

(K) Upregulated DEGs between ZsGreen+ versus ZsGreen− BECs (CD31$^+$) in the dura show a significant enrichment of Gene Ontology (GO) terms related to immune cell recruitment and adhesion.

(L) Upregulated DEGs between ZsGreen+ versus ZsGreen− skull B cells reveal immunological specialization. (Li) Upregulated DEGs were significantly enriched for GO terms such as antigen processing and ubiquitin proteasome system (UPS) degradation, and major histocompatibility complex class I (MHC class I) antigen processing and presentation. Many of the genes in these two GO terms are key antigen processing and presentation genes. String interactome analysis confirms that the genes in this GO term have been shown to interact. (Lii) Gene expression changes for key tolerogenic and inflammatory genes from the B cell cluster demonstrate that ZsGreen+ skull B cells display an upregulated tolerogenic transcriptional profile. (Liii) Pseudotime trajectory analysis comparing the expression of a tolerogenic module (*Ptpn22*, *Zbtb20*, *Cd274*) across the transition from pre-B to B cells. The expression of the tolerogenic module was significantly higher in ZsGreen+ cells compared with ZsGreen−.

All data are mean ± SEM with $n = 4$. $^*p \leq 0.05$, $^{**}p \leq 0.01$, and $^{***}p \leq 0.001$ by one-way ANOVA with Tukey's post hoc, Wilcoxon, or Student's *t* test. The top ten to twelve GO biological processes or reactome terms were selected based on a 0.01 false discovery rate (FDR) cutoff and sorted by nGenes.

See also Figures S4 and S5.

Please cite this article in press as: Chayama et al., Physiological brain clearance architecture revealed by neuronal protein tracing, Cell (2026), https://doi.org/10.1016/j.cell.2026.04.048

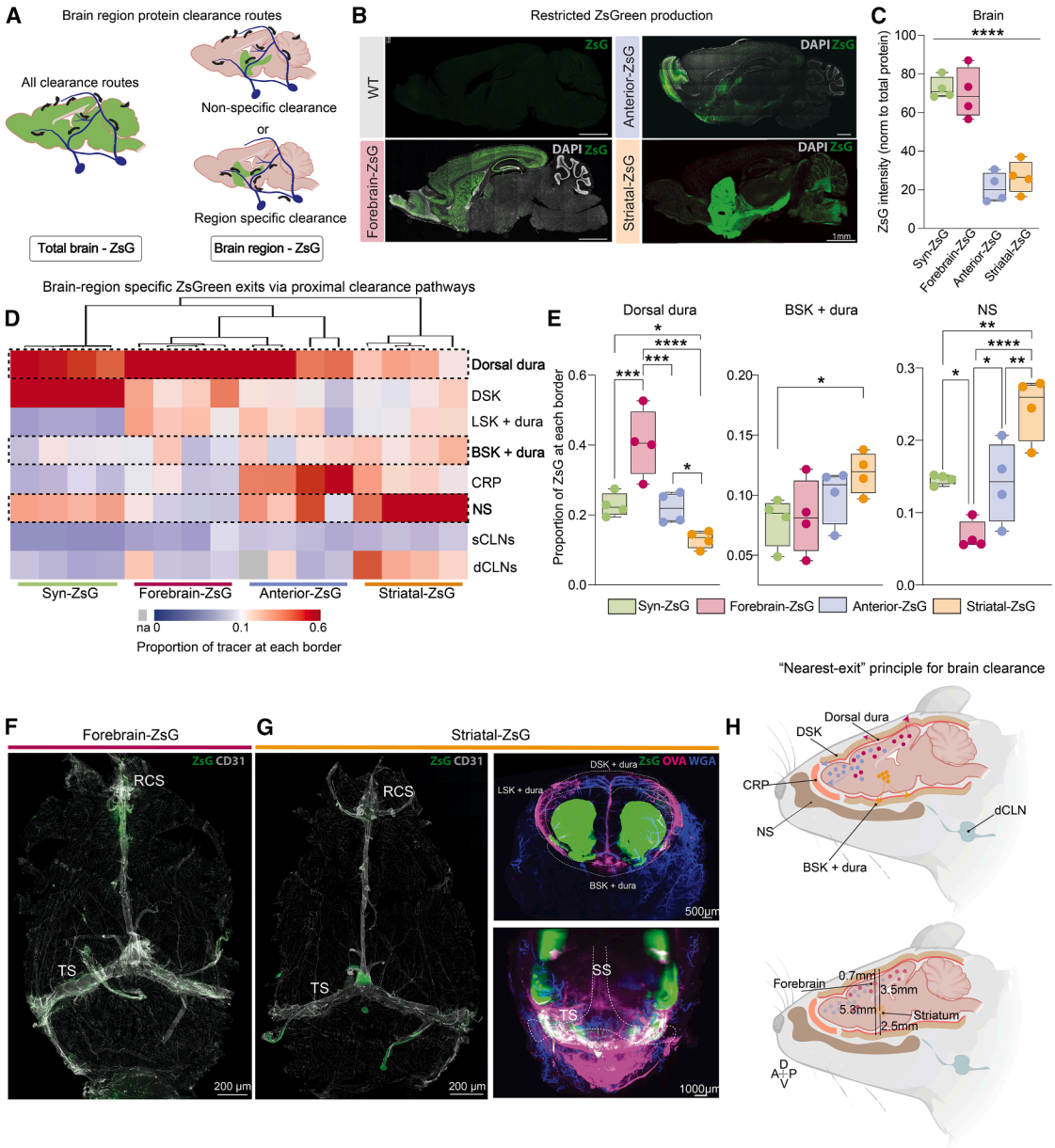

Figure 5. Brain waste clearance is regionally compartmentalized and follows a nearest exit principle

(A) Schematic comparing global neuronal labeling using Syn-ZsG mice (left) versus a restricted ZsGreen expression. The cartoon illustrates two possibilities for ZsGreen clearance through global non-specific (top) or region-specific pathways (bottom).

(B) Representative IHC analysis of restricted ZsG expression for 3 brain regions. Forebrain-ZsG (CaMKII-positive neurons), anterior-ZsG (forebrain and olfactory bulb GABA-ergic interneurons), and striatal-ZsG (striatal medium spiny neurons). IHC confirms restricted ZsGreen expression for each compared with PBS::WT controls.

(C) Fluorescent plate reader quantification of ZsGreen signal in the brain shows significantly different ZsGreen abundances across Syn-ZsG, forebrain-ZsG, anterior-ZsG, and striatal-ZsG paradigms.

(D) Heatmap of ZsGreen utilization (proportion of ZsGreen at a border/total ZsGreen across borders) from fluorescence plate reader analysis. Fluorescent intensities from bulk homogenates were normalized to total protein and respective ZsGreen abundance in the brain. Across all regionally restricted models, ZsGreen signal is enriched at borders proximal to the labeled region and reduced at more distal borders.

(E) Boxplots showing the proportion of ZsGreen detected at selected brain border compartments (dorsal dura, BSK + dura, and NS) across Syn-ZsG and regionally restricted labeling paradigms. Significant differences in border utilization were observed depending on the anatomical origin of ZsGreen, with enrichment at borders proximal to the labeled region.

(F) Representative IHC of dural whole mounts from forebrain-ZsG and striatal-ZsG mice demonstrates varied anatomical distributions of ZsGreen colocalizing with vascular structures (CD31).

(G) LSFM of whole CUBIC-cleared heads from striatal-ZsG mice with ICM-injected OVA-555. Top-down and side perspectives of the striatum-distal dorsal dura showing little ZsGreen signal in the dorsal dura of striatal-ZsG mice.

(legend continued on next page)

Please cite this article in press as: Chayama et al., Physiological brain clearance architecture revealed by neuronal protein tracing, Cell (2026), https://doi.org/10.1016/j.cell.2026.04.048

drainage in striatal-ZsG mice compared with forebrain-ZsG mice, while anterior-ZsG mice showed a strong bias toward cribriform plate drainage. Dural whole mounts and whole-head LSFM imaging provided visual confirmation of this pattern, revealing decreased ZsGreen in the dorsal dura and increased signal in the nasal cavity and basal skull in striatal-ZsG mice (Figures 5E–5G and S6B–S6E).

Having ruled out tracer duration as the source of divergence between ZsGreen and CSF tracers, we next asked whether matching the anatomical site of origin would eliminate this difference. We compared striatal-ZsG mice to mice receiving intraparenchymal OVA injections into the striatum (Str-Inj:OVA). IHC of brain sections confirmed OVA-647 injection at 1 h, with clearance evident by 24 h (Figure S6F). Plotting the proportion of OVA and ZsGreen at each drainage border in Str-Inj:OVA and striatal-ZsG mice, respectively, revealed that skull borders were underrepresented by OVA with substantially greater drainage to sCLNs (Figure S6G). This indicates that bolus injection, even when delivered directly into the parenchyma, overwhelms local border uptake capacity and shunts flow to cervical lymph nodes.

Together, these findings indicate that brain-derived protein clearance is regionally compartmentalized, with preferential drainage to proximal borders, supporting a "nearest exit" principle (Figure 5H).

Neuroinflammation and amyloid pathology differentially disrupt the clearance of brain-derived proteins

Having defined the architecture of physiological brain clearance, we next investigated how this system is altered under pathological conditions. We used two distinct and clinically relevant models: acute systemic inflammation induced by lipopolysaccharide (LPS) and the 5XFAD transgenic model[100] of amyloidosis and AD.

First, we examined the impact of acute inflammation. We i.p. injected Syn-ZsG mice with 3 mg/kg LPS, an endotoxin known to compromise the BBB and activate neuroimmune responses (Figure 6A).[101,102] As expected, LPS impaired BBB integrity, resulting in Cadaverin-647 tracer extravasation as well as neuroinflammation confirmed by GFAP$^+$ reactive astrogliosis (Figures 6B and S7A). Next, we investigated if LPS treatment modulated ZsGreen drainage. While ZsGreen levels within the brain remained unchanged compared with WT controls, clearance to major border exit routes, including the dorsal and basal skull and nasal cavity, was significantly reduced after LPS treatment (Figures 6C and 6D). Given the brain showed no difference in abundance and select brain borders displayed less ZsGreen, we hypothesized that the ZsGreen was inappropriately shunted through compromised vasculature into the blood (Figures S7B and S7C). Indeed, we quantified an increase in ZsGreen fluorescence in plasma with LPS (Figures 6E, S7D, and S7E). These findings suggest that acute neuroinflammation disrupts homeostatic drainage routes through brain borders, triggering a collapse of normal efflux pathways and shunting of neuronal proteins directly into peripheral circulation through a leaky vasculature.

To assess how a chronic, age-related stressor impacts brain clearance, we next turned to the 5XFAD mouse model, which develops early and aggressive amyloid pathology beginning at 2 months of age.[100] While these mice do not recapitulate all aspects of human AD, they represent a strong model for investigating how ZsGreen drainage across brain borders is affected by progressing neuropathology. We leveraged AAV-based expression of ZsGreen in neurons in WT and 5XFAD mice followed by biochemical analyses (Figure 6F). IHC analysis of brain sections and quantification of brain confirmed neuronal ZsGreen production and revealed that 5XFAD brains displayed substantial ZsGreen and Aβ_{42} accumulation relative to controls (Figures 6G–6I). Given ZsGreen's retention in the brain, we next investigated if brain borders had modulated uptake of ZsGreen. Indeed, nearly all brain borders showed significantly decreased ZsGreen levels in 5XFAD-ZsG mice compared with controls (Figure 6J). ZsGreen levels across brain borders did not correlate with Aβ_{42}: while ZsGreen drains across diverse brain borders, Aβ's unique biophysical properties and regional expression may favor dorsal dura efflux pathways.[27] Immunostaining of dural whole mounts confirmed Aβ_{42} at the dura with accumulation at bridging veins' exit points[103] (Figures 6K and S7F). This impairment in brain-to-border clearance was reflected in the periphery, where plasma ZsGreen was significantly lower in 5XFAD-ZsG mice compared with controls (Figure 6L). To verify that ZsGreen production did not alter endogenous Aβ_{42} distribution, we quantified Aβ_{42} levels across brain borders in 5XFAD-ZsG and 5XFAD and observed comparable patterns (Figure S7G). Finally, to assess how clearance impairments track with disease progression, we analyzed 5XFAD mice at 2 months of age (Figures 6M and S7H). ZsGreen efflux from brain to blood diminished from 2 to 7 months of age, and the degree of impairment correlated strongly with Aβ_{42} levels (Figures 6N and S7I).

Together, these findings demonstrate that when disease-relevant insults disrupt CNS protein clearance, they do so through fundamentally distinct mechanisms. Acute inflammation reroutes homeostatic drainage through a destabilized vasculature directly into the bloodstream. By contrast, amyloid pathology progressively obstructs brain protein drainage by trapping proteins within the parenchyma and blocking their access to border efflux routes, resulting in reduced clearance (Figure 6O).

DISCUSSION

In this study, we developed and validated a genetic system to track the clearance of neuron-derived proteins as they efflux from their site of origin in the brain to exit sites across CNS

(H) Schematic depicting proposed nearest-exit paradigm for brain waste clearance (top). Distances from the mid-forebrain and mid-striatum to dorsal and basal brain borders illustrate how anatomical proximity may bias drainage toward closer border compartments.

SS/BV, sagittal sinus/bridging veins; RCS, rostral confluence of sinus; TS, transverse sinus. All data are mean ± SEM with $n = 4$. *$p \leq 0.05$, **$p \leq 0.01$, and ***$p \leq 0.001$ by one-way ANOVA with Tukey's post hoc or Student's t test.

See also Figure S6.

Please cite this article in press as: Chayama et al., Physiological brain clearance architecture revealed by neuronal protein tracing, Cell (2026), https://doi.org/10.1016/j.cell.2026.04.048

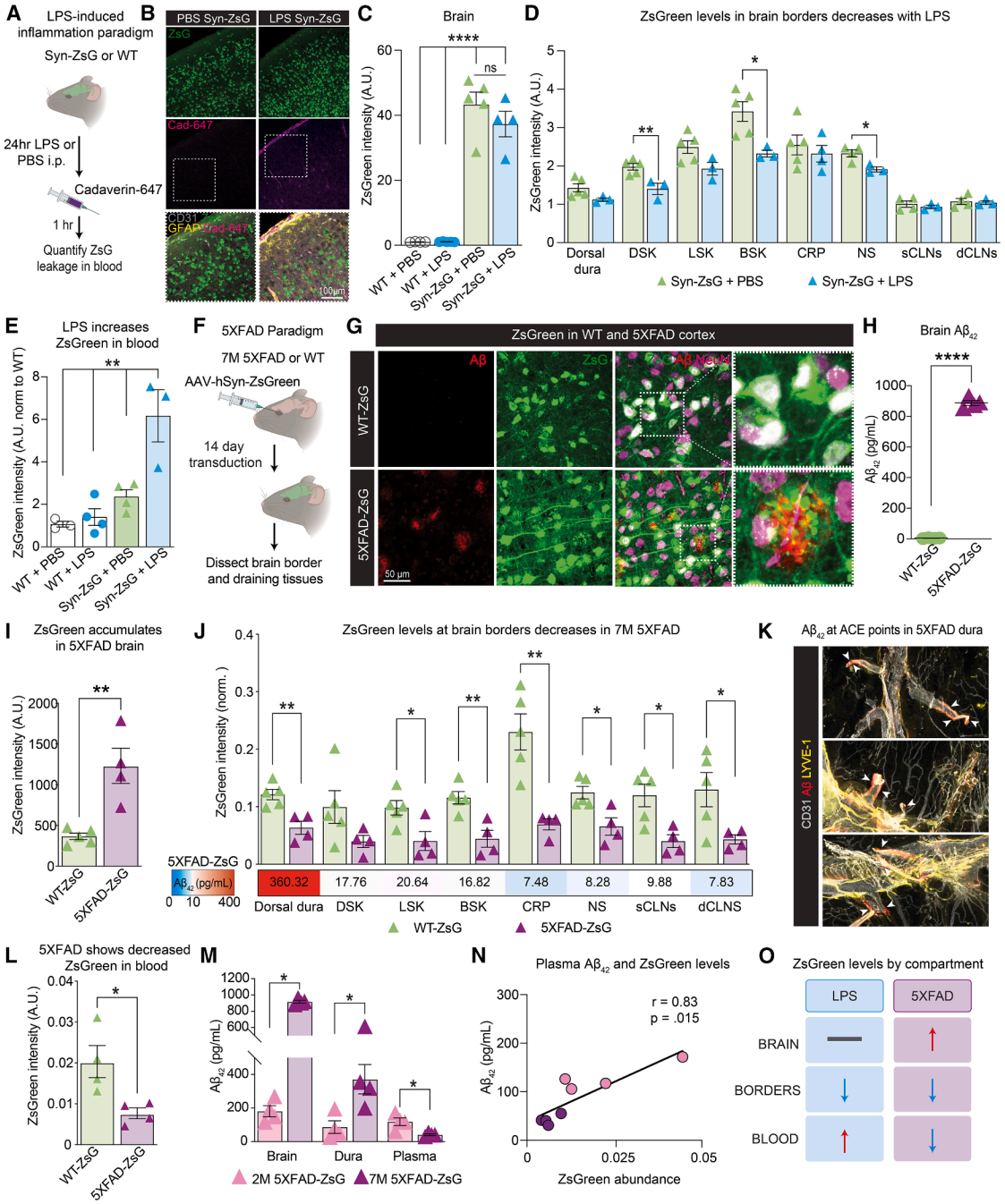

Figure 6. Neuroinflammation and neurodegenerative pathologies induce distinct forms of drainage dysfunction

(A) Schematic of the experimental paradigm for inducing acute inflammation. WT mice and Syn-ZsG mice (1 week after transduction) were given LPS (3 mg/kg) or PBS via intraperitoneal (i.p.) injection to induce acute neuroinflammation. After 24 h, mice were administered intravenous Cadaverin-647 tracer to assess LPS-induced sequelae and BBB compromise.

(B) IHC of brain sections from Syn-ZsG mice shows Cadaverin-647 extravasation in Syn-ZsG + LPS mice compared with Syn-ZsG + PBS controls.

(C) Fluorescent plate reader analysis demonstrates that LPS treatment does not significantly alter ZsGreen abundance within the brain.

(D) Fluorescent plate reader quantification of ZsGreen levels across brain borders and drainage sites from Syn-ZsG PBS or LPS-treated mice reveals an overall decrease in drainage to brain borders, with significant decreases across the DSK, BSK, and NS following LPS treatment.

(E) Fluorescent plate reader analysis demonstrates that LPS treatment significantly increases ZsGreen abundance in the blood plasma of Syn-ZsG mice.

(F) Schematic of the experimental paradigm for investigating how ZsGreen clearance is affected by amyloid pathology in the 5XFAD model. In 7- or 2-month-old 5XFAD mice, retroorbital AAV transduction of AAV::hSyn-ZsGreen-P2A-mCherry was performed. After 14 days of transduction, brain borders and drainage tissues were collected for biochemical analyses. WT::hSyn-ZsG (WT-ZsG) and 5XFAD::hSyn-ZsG (5XFAD-ZsG).

(legend continued on next page)

Please cite this article in press as: Chayama et al., Physiological brain clearance architecture revealed by neuronal protein tracing, Cell (2026), https://doi.org/10.1016/j.cell.2026.04.048

borders. Using this system, we reveal that neuron-derived protein drainage differs from routes predicted by injected tracers. We establish that physiological clearance follows a nearest exit principle for brain regions, exhibits distinct clearance kinetics across brain borders, is surveilled by select pro-tolerogenic border immune cells, and fails via distinct mechanisms in inflammation versus neurodegeneration. These findings support a framework where brain waste clearance is spatially compartmentalized and organized to deliver neuronal antigens from specific brain regions to corresponding border niches.

Our results help clarify long-standing discussions regarding the primary routes of CNS protein clearance.[4,6,32,35,71] We propose the divergence in clearance patterns observed between our ZsGreen paradigm and CSF-tracer studies reflects fundamental differences in how these approaches engage physiological pathways. We found that under physiological conditions, neuronal proteins primarily drain to dorsal and basal dura, skull, and nasal sites, with less prominent drainage to sCLNs and dCLNs.[4,6,32,35] This distribution differs from many studies using ICM-injected tracers, which report that the majority (typically >50%–80%) of infused tracers are recovered in the CLNs.[4,33,47,59,104,105] This discrepancy may stem from methodology where acute bolus or chronic CSF infusions may favor rapid flow to lymph nodes and bypass the brain,[47] whereas our steady-state tracing of protein from the brain highlights the importance of immune-rich "staging areas" in the dorsal dura[5,6,9,12,27,57,58] and skull[60–64] upstream of cervical lymph nodes. Our findings are consistent with immunopeptidomics studies demonstrating richer repertoires of CNS antigens in dura compared with lymph nodes.[106]

Critically, we demonstrate this discrepancy is not an artifact of tracer duration. Matching the chronicity of ZsGreen production with 14-day osmotic pump infusion of OVA into the CSF did not recapitulate the parenchymal drainage pattern. Instead, chronic CSF tracers still accumulated preferentially in cervical lymph nodes. This indicates that lymph node accumulation in tracer studies reflects the site of tracer introduction (CSF versus parenchyma) and dose (bolus versus continuous production). Consistently, intraparenchymal OVA injection into the striatum still substantially drained to sCLNs, unlike the drainage of striatal-ZsG mice.

By revealing neuron-derived proteins draining to both dorsal[5,6,27,57,58] and basal[9,54,59] aspects of the dura and skull, our findings suggest both routes mediate brain waste clearance and reveal an additional layer of spatial organization. Indeed, our neuron-derived tracing strategy reveals a previously unappreciated degree of spatial compartmentalization in brain clearance, indicating that "primary" routes of CNS clearance will depend on where the molecule in question originates in the brain. This clearance compartmentalization may also inform translational relevance. Given the evolutionary expansion of the human neocortex,[107,108] our nearest exit principle suggests a potentially greater functional role for dorsal clearance pathways in humans.[109,110] In addition, we found that border compartments differ in clearance kinetics, with skull-associated borders exhibiting slower outflow than dura, nasal cavity, and cribriform plate, indicating that CNS waste clearance is both spatially and temporally compartmentalized. Slower skull kinetics may facilitate prolonged antigen retention and immune surveillance.

Our flow and transcriptomic analyses suggest dorsal pathways play a significant role in immune surveillance relative to other brain borders.[5,6,9,12,27,57,58,60–64,111,112] For instance, despite similar overall ZsGreen exposure, BAMs[64,113,114] in dorsal dura sampled significantly more ZsGreen than BAMs in the nasal cavity. Yet, comparison of ZsGreen+ and ZsGreen− BAMs did not reveal distinct transcriptional signatures, suggesting extrinsic, anatomical differences or BAM positioning within each border regulates their antigen uptake. By contrast, we discovered a distinct transcriptional program in ZsGreen-sampling skull-resident B cells. ZsGreen+ B cells upregulated key components of the antigen processing and presentation pathway, while simultaneously expressing tolerogenic regulators, including PD-L1 protein. This "tolerogenic-presentation" profile supports a model where antigen-sampling skull B cells maintain immune tolerance to CNS-derived proteins. This concept extends recent studies showing that the skull marrow

(G) IHC of brain sections from WT-ZsG and 5XFAD-ZsG mice confirms that both genotypes have strong neuron-specific ZsGreen production, but only 5XFAD mice have amyloid pathology. Insets show ZsGreen puncta colocalized and associated with extracellular Aβ plaques.
(H) $A\beta_{42}$ ELISA analysis of brain homogenates confirms that 5XFAD-ZsG mice produce significantly more $A\beta_{42}$ compared with WT-ZsG healthy controls.
(I) Fluorescent plate reader analysis of ZsGreen abundance in brain homogenates reveals that 5XFAD-ZsG brains have significantly more ZsGreen compared with WT-ZsG mice.
(J) Fluorescent plate reader quantification of ZsGreen levels across brain borders and drainage sites of WT-ZsG or 5XFAD-ZsG mice reveal an overall decrease in drainage to nearly all brain borders in 5XFAD mice compared with healthy controls. In 5XFAD-ZsG tissues, corresponding $A\beta_{42}$ ELISA analysis demonstrates $A\beta_{42}$ mostly accumulates at the dorsal dura, despite global impairment in ZsGreen drainage across brain borders.
(K) Dural whole mounts from 7 M 5XFAD confirm $A\beta_{42}$ is highly abundant in the dorsal dura at distinct bridging veins exit points.
(L) Fluorescent plate reader analysis of ZsGreen abundance in blood plasma reveals 5XFAD-ZsG has significantly less ZsGreen in the blood compared with WT-ZsG mice.
(M) $A\beta_{42}$ ELISA analysis of 2- and 7-month-old 5XFAD-ZsG confirms that over time $A\beta_{42}$ accumulation is significantly increased in the brain and dura compartments but is decreased in the plasma.
(N) Correlation of ZsGreen and $A\beta_{42}$ abundance in 5XFAD-ZsG blood plasma mice reveals a significant positive correlation.
(O) Summary schematic showing the change in ZsGreen abundance in the brain, borders, and blood with acute inflammation (LPS) and with amyloid pathology (5XFAD). Neuroinflammation and neurodegenerative pathologies induce distinct forms of drainage dysfunction: while LPS shunts neuron-derived ZsGreen away from homeostatic drainage routes directly into the blood, likely via BBB compromise, Aβ pathology induces ZsGreen clogging and retention in the brain. DSK, dorsal skull; LSK, lateral skull; BSK, basal skull; CRP, cribriform plate; NS, nasal cavity; sCLNs and dCLNs, superficial and deep cervical lymph nodes.
All data are mean ± SEM with $n = 3–4$. $^*p \leq 0.05$, $^{**}p \leq 0.01$, $^{***}p \leq 0.001$, and $^{****}p \leq 0.0001$ by one-way ANOVA with Tukey's post hoc, Spearman's correlations, or Student's *t* test.
See also Figure S7.

hosts a reservoir of immature B cells capable of responding to local CNS cues.[61,63,64,115–117]

The heterogeneity in clearance kinetics and CNS immune surveillance across borders, together with the nearest exit hypothesis, opens new hypotheses for understanding regional vulnerability in disease. For instance, this patterning could function as a biological "zip code" system, ensuring that self-antigens from a specific neuronal neighborhood are consistently delivered to an immune niche at the corresponding brain border.[63,106,111,114] We hypothesize that in aging and disease, these precise pathways can degrade, effectively "scrambling" these zip codes. Expanding on prior studies, we found that neuroinflammation and amyloid pathology dysregulate brain clearance via distinct mechanisms.[25,27,30,38,42,118–120] Specifically, acute inflammation shunts brain-derived proteins into the blood via vascular leakage, while amyloid pathology causes parenchyma retention and obstruction of border exits. Both mechanisms could promote dysregulated neuroimmunity. For example, leakage may misroute brain antigens to the peripheral immune system rather than the proper pro-tolerogenic brain borders,[57,64] and retention leads to a loss of antigen drainage to and education at borders.[106] Further, this model could explain how the selective failure of clearance pathways servicing specific brain regions could lead to localized buildup of toxic proteins, initiating a cascade of pathologies characteristic of neurodegenerative disorders.

Overall, by developing a genetic system to trace the *in vivo* distribution of brain-derived proteins, we map the brain's physiological clearance architecture, revealing preferred drainage pathways, distinct border immune interfaces, and mechanisms of dysfunction in disease.

Limitations of the study

While our approach provides significant advantages over traditional tracer methods, limitations remain. First, our findings are in mice, owing to the need for genetic manipulation. Though conservation of meningeal lymphatics between rodents and humans has been shown, the precise anatomical flow patterns may differ in primates, necessitating future validation of these findings in non-human primate or human tissue studies.[44,46] Second, although we validated our findings with the endogenous proteome (Syn-PheRS),[90] ZsGreen is an exogenous protein that can form tetramers. Third, while Cre immunostaining and scRNA-seq of border tissues confirmed brain-restricted Cre expression, AAV-PHP.eB can transduce extra-CNS neurons (e.g., spinal cord and dorsal root ganglia). Finally, steady-state accumulation does not equal clearance rate. We addressed this with pulse-chase kinetics, though decay rates reflect combined local degradation and efflux, which cannot be fully disentangled. Complementary live imaging will be needed to capture acute temporal dynamics of CNS waste clearance.

RESOURCE AVAILABILITY

Lead contact

Requests for further information and resources should be directed to and will be fulfilled by the lead contact, Andrew C. Yang (andrew.yang@gladstone.ucsf.edu).

Materials availability

This study did not generate any new, unique reagents.

Data and code availability

- Raw sequencing data are available in the NCBI Sequence Read Archive (SRA) under BioProject accession number SRP599291.
- This paper does not report original code.
- Any additional information in this paper is available from the lead contact upon request.

ACKNOWLEDGMENTS

This research was supported by the National Institutes of Health (DP5OD033381), the National Institute of Neurological Disorders and Stroke (1R01NS128909 and 1RF1NS139975), the Alzheimer's Association (ADSF-24-1345199-C), the Burroughs Wellcome Fund Career Awards at the Scientific Interface, the Ludwig Family Foundation, the Longevity Impetus Grant from Norn Group, the UCSF Sandler Program for Breakthrough Biomedical Research New Frontier Research Award, and the Dolby Family. Y.C. is employed by Daiichi Sankyo Co., Ltd., and was a visiting scholar. M.B., A.E., and Z.I.K. were funded by the Deutsche Forschungsgemeinschaft (DFG) under Germany's Excellence Strategy within Munich Cluster for Systems Neurology (EXC 2145 SyNergy – ID 390857198 and CRC1744, DFG, German Research Foundation). We thank Mylinh Bernardi, Felicia Miller, and Horng-Ru Lin of the Gladstone Genomics Core for their assistance. We also thank participants of the 2024 "Brainwashing: Where Do We Stand on It?" meeting and 2025 CSHL Brain Barriers meeting, Robert Thorne, and members of the Yang laboratory for their feedback and support.

AUTHOR CONTRIBUTIONS

A.C.Y., Y.C., and N.R.R. conceptualized the study. Y.C. and N.R.R. led experiments, including immunohistochemical stains and imaging, flow cytometry, brain border dissections, scRNA-seq, and fluorescence quantifications, with the support of M.R., S.N., B.D., D.P., Z.Z., A.A., J.B., H.Z., S.G.T., S.D., and P.-Y.S. N.R.R. and A.C.Y. wrote the manuscript with input from all authors. A.E., Z.I.K., Y.-H.F., Y.H., and A.C.Y. supervised the study.

DECLARATION OF INTERESTS

The authors declare no competing interests.

STAR★METHODS

Detailed methods are provided in the online version of this paper and include the following:

- KEY RESOURCES TABLE
- EXPERIMENTAL MODEL AND STUDY PARTICIPANT DETAILS
  - Animals
  - AAV Production
  - Retroorbital Injection
  - Intracisterna magna (ICM) injections of tracers
  - Intrastriatal injection of OVA
  - Chronic CSF-infusion of OVA
  - Endogenous labeling of neuronal proteomes
- METHOD DETAILS
  - Cu-Click for IHC
  - In-gel fluorescence detection of azide-modified proteins
  - Immunohistochemistry
  - Tissue Clearing and Light Sheet Fluorescence Imaging
  - Tissue homogenization and plate reader quantification
  - Western blot
  - Flow cytometry
  - Single-Cell RNA Sequencing
  - Blood-Brain Barrier Permeability Assay
  - LPS-induced inflammation

SUPPLEMENTAL INFORMATION

Supplemental information can be found online at https://doi.org/10.1016/j.cell.2026.04.048.

Received: July 15, 2025
Revised: February 13, 2026
Accepted: April 29, 2026

REFERENCES

1. Murphy, J.B., and Sturm, E. (1923). Conditions Determining the Transplantability of Tissues in the Brain. J. Exp. Med. *38*, 183–197. https://doi.org/10.1084/jem.38.2.183.
2. Attwell, D., and Laughlin, S.B. (2001). An energy budget for signaling in the grey matter of the brain. J. Cereb. Blood Flow Metab. *21*, 1133–1145. https://doi.org/10.1097/00004647-200110000-00001.
3. Harris, J.J., Jolivet, R., and Attwell, D. (2012). Synaptic energy use and supply. Neuron *75*, 762–777. https://doi.org/10.1016/j.neuron.2012.08.019.
4. Iliff, J.J., Wang, M., Liao, Y., Plogg, B.A., Peng, W., Gundersen, G.A., Benveniste, H., Vates, G.E., Deane, R., Goldman, S.A., et al. (2012). A paravascular pathway facilitates CSF flow through the brain parenchyma and the clearance of interstitial solutes, including amyloid beta. Sci. Transl. Med. *4*, 147ra111. https://doi.org/10.1126/scitranslmed.3003748.
5. Aspelund, A., Antila, S., Proulx, S.T., Karlsen, T.V., Karaman, S., Detmar, M., Wiig, H., and Alitalo, K. (2015). A dural lymphatic vascular system that drains brain interstitial fluid and macromolecules. J. Exp. Med. *212*, 991–999. https://doi.org/10.1084/jem.20142290.
6. Louveau, A., Smirnov, I., Keyes, T.J., Eccles, J.D., Rouhani, S.J., Peske, J.D., Derecki, N.C., Castle, D., Mandell, J.W., Lee, K.S., et al. (2015). Structural and functional features of central nervous system lymphatic vessels. Nature *523*, 337–341. https://doi.org/10.1038/nature14432.
7. Smets, N.G., van der Panne, S.A., Strijkers, G.J., and Bakker, E.N.T.P. (2024). Perivascular spaces around arteries exceed perivenous spaces in the mouse brain. Sci. Rep. *14*, 17655. https://doi.org/10.1038/s41598-024-67885-y.
8. Bojarskaite, L., Nafari, S., Ravnanger, A.K., Frey, M.M., Skauli, N., Åbjørsbråten, K.S., Roth, L.C., Amiry-Moghaddam, M., Nagelhus, E.A., Ottersen, O.P., et al. (2024). Role of aquaporin-4 polarization in extracellular solute clearance. Fluids Barriers CNS *21*, 28. https://doi.org/10.1186/s12987-024-00527-7.
9. Ahn, J.H., Cho, H., Kim, J.H., Kim, S.H., Ham, J.S., Park, I., Suh, S.H., Hong, S.P., Song, J.H., Hong, Y.K., et al. (2019). Meningeal lymphatic vessels at the skull base drain cerebrospinal fluid. Nature *572*, 62–66. https://doi.org/10.1038/s41586-019-1419-5.
10. Oliver, G., Kipnis, J., Randolph, G.J., and Harvey, N.L. (2020). The Lymphatic Vasculature in the 21(st) Century: Novel Functional Roles in Homeostasis and Disease. Cell *182*, 270–296. https://doi.org/10.1016/j.cell.2020.06.039.
11. Hannocks, M.J., Pizzo, M.E., Huppert, J., Deshpande, T., Abbott, N.J., Thorne, R.G., and Sorokin, L. (2018). Molecular characterization of perivascular drainage pathways in the murine brain. J. Cereb. Blood Flow Metab. *38*, 669–686. https://doi.org/10.1177/0271678X17749689.
12. Zhang, Q., Niu, Y., Li, Y., Xia, C., Chen, Z., Chen, Y., and Feng, H. (2025). Meningeal lymphatic drainage: novel insights into central nervous system disease. Signal Transduct. Target. Ther. *10*, 142. https://doi.org/10.1038/s41392-025-02177-z.
13. Lun, M.P., Monuki, E.S., and Lehtinen, M.K. (2015). Development and functions of the choroid plexus-cerebrospinal fluid system. Nat. Rev. Neurosci. *16*, 445–457. https://doi.org/10.1038/nrn3921.
14. Engelhardt, B., and Coisne, C. (2011). Fluids and barriers of the CNS establish immune privilege by confining immune surveillance to a two-walled castle moat surrounding the CNS castle. Fluids Barriers CNS *8*, 4. https://doi.org/10.1186/2045-8118-8-4.
15. Koh, L., Zakharov, A., and Johnston, M. (2005). Integration of the subarachnoid space and lymphatics: is it time to embrace a new concept of cerebrospinal fluid absorption? Cerebrospinal Fluid Res. *2*, 6. https://doi.org/10.1186/1743-8454-2-6.
16. Kida, S., Pantazis, A., and Weller, R.O. (1993). CSF drains directly from the subarachnoid space into nasal lymphatics in the rat. Anatomy, histology and immunological significance. Neuropathol. Appl. Neurobiol. *19*, 480–488. https://doi.org/10.1111/j.1365-2990.1993.tb00476.x.
17. Upton, M.L., and Weller, R.O. (1985). The morphology of cerebrospinal fluid drainage pathways in human arachnoid granulations. J. Neurol. Surg. *63*, 867–875. https://doi.org/10.3171/jns.1985.63.6.0867.
18. Rennels, M.L., Gregory, T.F., Blaumanis, O.R., Fujimoto, K., and Grady, P.A. (1985). Evidence for a 'paravascular' fluid circulation in the mammalian central nervous system, provided by the rapid distribution of tracer protein throughout the brain from the subarachnoid space. Brain Res. *326*, 47–63. https://doi.org/10.1016/0006-8993(85)91383-6.
19. Bradbury, M.W., and Westrop, R.J. (1983). Factors influencing exit of substances from cerebrospinal fluid into deep cervical lymph of the rabbit. J. Physiol. *339*, 519–534. https://doi.org/10.1113/jphysiol.1983.sp014731.
20. Dani, N., Herbst, R.H., Habib, N., Head, J., Dionne, D., Nguyen, L., McCabe, C., Cui, J., Shipley, F.B., Jang, A., et al. (2019). A cellular and spatial map of the choroid plexus across brain ventricles and ages. Cell *184*, 3056–3074.e21.
21. Lehtinen, M.K., Bjornsson, C.S., Dymecki, S.M., Gilbertson, R.J., Holtzman, D.M., and Monuki, E.S. (2013). The choroid plexus and cerebrospinal fluid: emerging roles in development, disease, and therapy. J. Neurosci. *33*, 17553–17559. https://doi.org/10.1523/JNEUROSCI.3258-13.2013.
22. Pizzo, M.E., Wolak, D.J., Kumar, N.N., Brunette, E., Brunnquell, C.L., Hannocks, M.J., Abbott, N.J., Meyerand, M.E., Sorokin, L., Stanimirovic, D.B., et al. (2018). Intrathecal antibody distribution in the rat brain: surface diffusion, perivascular transport and osmotic enhancement of delivery. J. Physiol. *596*, 445–475. https://doi.org/10.1113/JP275105.
23. Pollock, H., Hutchings, M., Weller, R.O., and Zhang, E.T. (1997). Perivascular spaces in the basal ganglia of the human brain: their relationship to lacunes. J. Anat. *191*, 337–346. https://doi.org/10.1046/j.1469-7580.1997.19130337.x.
24. Murdock, M.H., Yang, C.Y., Sun, N., Pao, P.C., Blanco-Duque, C., Kahn, M.C., Kim, T., Lavoie, N.S., Victor, M.B., Islam, M.R., et al. (2024). Multisensory gamma stimulation promotes glymphatic clearance of amyloid. Nature *627*, 149–156. https://doi.org/10.1038/s41586-024-07132-6.
25. Nedergaard, M., and Goldman, S.A. (2020). Glymphatic failure as a final common pathway to dementia. Science *370*, 50–56. https://doi.org/10.1126/science.abb8739.
26. Kress, B.T., Iliff, J.J., Xia, M., Wang, M., Wei, H.S., Zeppenfeld, D., Xie, L., Kang, H., Xu, Q., Liew, J.A., et al. (2014). Impairment of paravascular clearance pathways in the aging brain. Ann. Neurol. *76*, 845–861. https://doi.org/10.1002/ana.24271.
27. Da Mesquita, S., Louveau, A., Vaccari, A., Smirnov, I., Cornelison, R.C., Kingsmore, K.M., Contarino, C., Onengut-Gumuscu, S., Farber, E., Raper, D., et al. (2018). Functional aspects of meningeal lymphatics in

ageing and Alzheimer's disease. Nature *560*, 185–191. https://doi.org/10.1038/s41586-018-0368-8.

28. Ding, X.B., Wang, X.X., Xia, D.H., Liu, H., Tian, H.Y., Fu, Y., Chen, Y.K., Qin, C., Wang, J.Q., Xiang, Z., et al. (2021). Impaired meningeal lymphatic drainage in patients with idiopathic Parkinson's disease. Nat. Med. *27*, 411–418. https://doi.org/10.1038/s41591-020-01198-1.
29. Wen, Y.R., Yang, J.H., Wang, X., and Yao, Z.B. (2018). Induced dural lymphangiogenesis facilities soluble amyloid-beta clearance from brain in a transgenic mouse model of Alzheimer's disease. Neural Regen. Res. *13*, 709–716. https://doi.org/10.4103/1673-5374.230299.
30. Zamani, A., Walker, A.K., Rollo, B., Ayers, K.L., Farah, R., O'Brien, T.J., and Wright, D.K. (2022). Impaired glymphatic function in the early stages of disease in a TDP-43 mouse model of amyotrophic lateral sclerosis. Transl. Neurodegener. *11*, 17. https://doi.org/10.1186/s40035-022-00291-4.
31. Wang, L., Zhang, Y., Zhao, Y., Marshall, C., Wu, T., and Xiao, M. (2019). Deep cervical lymph node ligation aggravates AD-like pathology of APP/PS1 mice. Brain Pathol. *29*, 176–192. https://doi.org/10.1111/bpa.12656.
32. Ma, Q., Ineichen, B.V., Detmar, M., and Proulx, S.T. (2017). Outflow of cerebrospinal fluid is predominantly through lymphatic vessels and is reduced in aged mice. Nat. Commun. *8*, 1434. https://doi.org/10.1038/s41467-017-01484-6.
33. Benveniste, H., Liu, X., Koundal, S., Sanggaard, S., Lee, H., and Wardlaw, J. (2019). The Glymphatic System and Waste Clearance with Brain Aging: A Review. Gerontology *65*, 106–119. https://doi.org/10.1159/000490349.
34. Voumvourakis, K.I., Sideri, E., Papadimitropoulos, G.N., Tsantzali, I., Hewlett, P., Kitsos, D., Stefanou, M., Bonakis, A., Giannopoulos, S., Tsivgoulis, G., et al. (2023). The Dynamic Relationship between the Glymphatic System, Aging, Memory, and Sleep. Biomedicines *11*, 2092. https://doi.org/10.3390/biomedicines11082092.
35. Mestre, H., Mori, Y., and Nedergaard, M. (2020). The Brain's Glymphatic System: Current Controversies. Trends Neurosci. *43*, 458–466. https://doi.org/10.1016/j.tins.2020.04.003.
36. Hablitz, L.M., and Nedergaard, M. (2021). The glymphatic system: A novel component of fundamental neurobiology. J. Neurosci. *41*, 7698–7711. https://doi.org/10.1523/JNEUROSCI.0619-21.2021.
37. Louveau, A., Plog, B.A., Antila, S., Alitalo, K., Nedergaard, M., and Kipnis, J. (2017). Understanding the functions and relationships of the glymphatic system and meningeal lymphatics. J. Clin. Investig. *127*, 3210–3219. https://doi.org/10.1172/JCI90603.
38. Hauglund, N.L., Andersen, M., Tokarska, K., Radovanovic, T., Kjaerby, C., Sørensen, F.L., Bojarowska, Z., Untiet, V., Ballestero, S.B., Kolmos, M.G., et al. (2025). Norepinephrine-mediated slow vasomotion drives glymphatic clearance during sleep. Cell *188*, 606–622.e17. https://doi.org/10.1016/j.cell.2024.11.027.
39. Harrison, I.F., Ismail, O., Machhada, A., Colgan, N., Ohene, Y., Nahavandi, P., Ahmed, Z., Fisher, A., Meftah, S., Murray, T.K., et al. (2020). Impaired glymphatic function and clearance of tau in an Alzheimer's disease model. Brain *143*, 2576–2593. https://doi.org/10.1093/brain/awaa179.
40. Peng, W., Achariyar, T.M., Li, B., Liao, Y., Mestre, H., Hitomi, E., Regan, S., Kasper, T., Peng, S., Ding, F., et al. (2016). Suppression of glymphatic fluid transport in a mouse model of Alzheimer's disease. Neurobiol. Dis. *93*, 215–225. https://doi.org/10.1016/j.nbd.2016.05.015.
41. Chen, X., Liu, X., Koundal, S., Elkin, R., Zhu, X., Monte, B., Xu, F., Dai, F., Pedram, M., Lee, H., et al. (2022). Cerebral amyloid angiopathy is associated with glymphatic transport reduction and time-delayed solute drainage along the neck arteries. Nat Aging *2*, 214–223. https://doi.org/10.1038/s43587-022-00181-4.
42. Xie, L., Kang, H., Xu, Q., Chen, M.J., Liao, Y., Thiyagarajan, M., O'Donnell, J., Christensen, D.J., Nicholson, C., Iliff, J.J., et al. (2013). Sleep drives metabolite clearance from the adult brain. Science *342*, 373–377. https://doi.org/10.1126/science.1241224.
43. Da Mesquita, S., Papadopoulos, Z., Dykstra, T., Brase, L., Farias, F.G., Wall, M., Jiang, H., Kodira, C.D., de Lima, K.A., Herz, J., et al. (2021). Meningeal lymphatics affect microglia responses and anti-Abeta immunotherapy. Nature *593*, 255–260. https://doi.org/10.1038/s41586-021-03489-0.
44. Keil, S.A., Jansson, D., Braun, M., and Iliff, J.J. (2025). Glymphatic dysfunction in Alzheimer's disease: A critical appraisal. Science *389*, eadv8269. https://doi.org/10.1126/science.adv8269.
45. Smyth, L.C.D., and Kipnis, J. (2025). Redefining CNS immune privilege. Nat. Rev. Immunol. *25*, 766–775. https://doi.org/10.1038/s41577-025-01175-0.
46. Jacob, L., de Brito Neto, J., Lenck, S., Corcy, C., Benbelkacem, F., Geraldo, L.H., Xu, Y., Thomas, J.M., El Kamouh, M.R., Spajer, M., et al. (2022). Conserved meningeal lymphatic drainage circuits in mice and humans. J. Exp. Med. *219*. https://doi.org/10.1084/jem.20220035.
47. Ma, Q., Ries, M., Decker, Y., Müller, A., Riner, C., Bücker, A., Fassbender, K., Detmar, M., and Proulx, S.T. (2019). Rapid lymphatic efflux limits cerebrospinal fluid flow to the brain. Acta Neuropathol. *137*, 151–165. https://doi.org/10.1007/s00401-018-1916-x.
48. Albargothy, N.J., Johnston, D.A., MacGregor-Sharp, M., Weller, R.O., Verma, A., Hawkes, C.A., and Carare, R.O. (2018). Convective influx/glymphatic system: tracers injected into the CSF enter and leave the brain along separate periarterial basement membrane pathways. Acta Neuropathol. *136*, 139–152. https://doi.org/10.1007/s00401-018-1862-7.
49. Ringstad, G., Valnes, L.M., Dale, A.M., Pripp, A.H., Vatnehol, S.A.S., Emblem, K.E., Mardal, K.A., and Eide, P.K. (2018). Brain-wide glymphatic enhancement and clearance in humans assessed with MRI. JCI Insight *3*, e121537. https://doi.org/10.1172/jci.insight.121537.
50. Melin, E., Eide, P.K., and Ringstad, G. (2020). In vivo assessment of cerebrospinal fluid efflux to nasal mucosa in humans. Sci. Rep. *10*, 14974. https://doi.org/10.1038/s41598-020-72031-5.
51. van Osch, M.J.P., Wåhlin, A., Scheyhing, P., Mossige, I., Hirschler, L., Eklund, A., Mogensen, K., Gomolka, R., Radbruch, A., Qvarlander, S., et al. (2024). Human brain clearance imaging: Pathways taken by magnetic resonance imaging contrast agents after administration in cerebrospinal fluid and blood. NMR Biomed. *37*, e5159. https://doi.org/10.1002/nbm.5159.
52. Kwon, S., Janssen, C.F., Velasquez, F.C., and Sevick-Muraca, E.M. (2017). Fluorescence imaging of lymphatic outflow of cerebrospinal fluid in mice. J. Immunol. Methods *449*, 37–43. https://doi.org/10.1016/j.jim.2017.06.010.
53. Jiang-Xie, L.F., Drieu, A., Bhasiin, K., Quintero, D., Smirnov, I., and Kipnis, J. (2024). Neuronal dynamics direct cerebrospinal fluid perfusion and brain clearance. Nature *627*, 157–164. https://doi.org/10.1038/s41586-024-07108-6.
54. Jin, H., Yoon, J.H., Hong, S.P., Hwang, Y.S., Yang, M.J., Choi, J., Kang, H.J., Baek, S.E., Jin, C., Jung, J., et al. (2025). Increased CSF drainage by non-invasive manipulation of cervical lymphatics. Nature *643*, 755–767. https://doi.org/10.1038/s41586-025-09052-5.
55. Proulx, S.T. (2021). Cerebrospinal fluid outflow: a review of the historical and contemporary evidence for arachnoid villi, perineural routes, and dural lymphatics. Cell. Mol. Life Sci. *78*, 2429–2457. https://doi.org/10.1007/s00018-020-03706-5.
56. Zhou, Y., Ran, W., Luo, Z., Wang, J., Fang, M., Wei, K., Sun, J., and Lou, M. (2022). Impaired peri-olfactory cerebrospinal fluid clearance is associated with ageing, cognitive decline and dyssomnia. EBiomedicine *86*, 104381. https://doi.org/10.1016/j.ebiom.2022.104381.
57. Rustenhoven, J., Drieu, A., Mamuladze, T., de Lima, K.A., Dykstra, T., Wall, M., Papadopoulos, Z., Kanamori, M., Salvador, A.F., Baker, W., et al. (2021). Functional characterization of the dural sinuses as a

neuroimmune interface. Cell *184*, 1000–1016.e27. https://doi.org/10.1016/j.cell.2020.12.040.

58. Fitzpatrick, Z., Ghabdan Zanluqui, N., Rosenblum, J.S., Tuong, Z.K., Lee, C.Y.C., Chandrashekhar, V., Negro-Demontel, M.L., Stewart, A.P., Posner, D.A., Buckley, M., et al. (2024). Venous-plexus-associated lymphoid hubs support meningeal humoral immunity. Nature *628*, 612–619. https://doi.org/10.1038/s41586-024-07202-9.

59. Yoon, J.-H., Jin, H., Kim, H.J., Hong, S.P., Yang, M.J., Ahn, J.H., Kim, Y.-C., Seo, J., Lee, Y., McDonald, D.M., et al. (2024). Nasopharyngeal lymphatic plexus is a hub for cerebrospinal fluid drainage. Nature *625*, 768–777. https://doi.org/10.1038/s41586-023-06899-4.

60. Herisson, F., Frodermann, V., Courties, G., Rohde, D., Sun, Y., Vandoorne, K., Wojtkiewicz, G.R., Masson, G.S., Vinegoni, C., Kim, J., et al. (2018). Direct vascular channels connect skull bone marrow and the brain surface enabling myeloid cell migration. Nat. Neurosci. *21*, 1209–1217. https://doi.org/10.1038/s41593-018-0213-2.

61. Mazzitelli, J.A., Smyth, L.C.D., Cross, K.A., Dykstra, T., Sun, J., Du, S., Mamuladze, T., Smirnov, I., Rustenhoven, J., and Kipnis, J. (2022). Cerebrospinal fluid regulates skull bone marrow niches via direct access through dural channels. Nat. Neurosci. *25*, 555–560. https://doi.org/10.1038/s41593-022-01029-1.

62. Kolabas, Z.I., Kuemmerle, L.B., Perneczky, R., Förstera, B., Ulukaya, S., Ali, M., Kapoor, S., Bartos, L.M., Büttner, M., Caliskan, O.S., et al. (2023). Distinct molecular profiles of skull bone marrow in health and neurological disorders. Cell *186*, 3706–3725.e29. https://doi.org/10.1016/j.cell.2023.07.009.

63. Brioschi, S., Wang, W.-L., Peng, V., Wang, M., Shchukina, I., Greenberg, Z.J., Bando, J.K., Jaeger, N., Czepielewski, R.S., Swain, A., et al. (2021). Heterogeneity of meningeal B cells reveals a lymphopoietic niche at the CNS borders. Science *373*, eabf9277. https://doi.org/10.1126/science.abf9277.

64. Cugurra, A., Mamuladze, T., Rustenhoven, J., Dykstra, T., Beroshvili, G., Greenberg, Z.J., Baker, W., Papadopoulos, Z., Drieu, A., Blackburn, S., et al. (2021). Skull and vertebral bone marrow are myeloid cell reservoirs for the meninges and CNS parenchyma. Science *373*, eabf7844. https://doi.org/10.1126/science.abf7844.

65. Norwood, J.N., Zhang, Q., Card, D., Craine, A., Ryan, T.M., and Drew, P.J. (2019). Anatomical basis and physiological role of cerebrospinal fluid transport through the murine cribriform plate. eLife *8*, e44278. https://doi.org/10.7554/eLife.44278.

66. Weller, R.O., Sharp, M.M., Christodoulides, M., Carare, R.O., and Møllgård, K. (2018). The meninges as barriers and facilitators for the movement of fluid, cells and pathogens related to the rodent and human CNS. Acta Neuropathol. *135*, 363–385. https://doi.org/10.1007/s00401-018-1809-z.

67. Laman, J.D., and Weller, R.O. (2013). Drainage of cells and soluble antigen from the CNS to regional lymph nodes. J. Neuroimmune Pharmacol. *8*, 840–856. https://doi.org/10.1007/s11481-013-9470-8.

68. Koh, L., Zakharov, A., Nagra, G., Armstrong, D., Friendship, R., and Johnston, M. (2006). Development of cerebrospinal fluid absorption sites in the pig and rat: connections between the subarachnoid space and lymphatic vessels in the olfactory turbinates. Anat. Embryol. *211*, 335–344. https://doi.org/10.1007/s00429-006-0085-1.

69. Johnston, M., Zakharov, A., Koh, L., and Armstrong, D. (2005). Subarachnoid injection of Microfil reveals connections between cerebrospinal fluid and nasal lymphatics in the non-human primate. Neuropathology Appl. Neurobio. *31*, 632–640. https://doi.org/10.1111/j.1365-2990.2005.00679.x.

70. Mollanji, R., Bozanovic-Sosic, R., Zakharov, A., Makarian, L., and Johnston, M.G. (2002). Blocking cerebrospinal fluid absorption through the cribriform plate increases resting intracranial pressure. Am. J. Physiol., Regul. Integr. Comp. Physiol. *282*, R1593–R1599. https://doi.org/10.1152/ajpregu.00695.2001.

71. Walter, B.A., Valera, V.A., Takahashi, S., and Ushiki, T. (2006). The olfactory route for cerebrospinal fluid drainage into the peripheral lymphatic system. Neuropathol. Appl. Neurobiol. *32*, 388–396. https://doi.org/10.1111/j.1365-2990.2006.00737.x.

72. Decker, Y., Krämer, J., Xin, L., Müller, A., Scheller, A., Fassbender, K., and Proulx, S.T. (2022). Magnetic resonance imaging of cerebrospinal fluid outflow after low-rate lateral ventricle infusion in mice. JCI Insight *7*, e150881. https://doi.org/10.1172/jci.insight.150881.

73. Raghunandan, A., Ladron-de-Guevara, A., Tithof, J., Mestre, H., Du, T., Nedergaard, M., Thomas, J.H., and Kelley, D.H. (2021). Bulk flow of cerebrospinal fluid observed in periarterial spaces is not an artifact of injection. eLife *10*, e65958. https://doi.org/10.7554/eLife.65958.

74. Gahn-Martinez, D., Giannetto, M., Chang, E., Beam, N., Tobin, P., Plá, V., and Nedergaard, M. (2025). Chronic Intraventricular Cannulation for the Study of Glymphatic Transport. eNeuro *12*. ENEURO.0537–ENEU24.2025. https://doi.org/10.1523/ENEURO.0537-24.2025.

75. Kiviniemi, V., Wang, X., Korhonen, V., Keinänen, T., Tuovinen, T., Autio, J., LeVan, P., Keilholz, S., Zang, Y.F., Hennig, J., et al. (2016). Ultra-fast magnetic resonance encephalography of physiological brain activity - Glymphatic pulsation mechanisms? J. Cereb. Blood Flow Metab. *36*, 1033–1045. https://doi.org/10.1177/0271678X15622047.

76. Betsholtz, C., Engelhardt, B., Koh, G.Y., McDonald, D.M., Proulx, S.T., and Siegenthaler, J. (2024). Advances and controversies in meningeal biology. Nat. Neurosci. *27*, 2056–2072. https://doi.org/10.1038/s41593-024-01701-8.

77. Papadopoulos, Z., Smyth, L.C.D., Smirnov, I., Gibson, D.A., Herz, J., and Kipnis, J. (2025). Differential impact of lymphatic outflow pathways on cerebrospinal fluid homeostasis. J. Exp. Med. *222*, e20241752. https://doi.org/10.1084/jem.20241752.

78. Ayyappan, K., Unger, L., Kitchen, P., Bill, R.M., and Salman, M.M. (2026). Measuring glymphatic function: Assessing the toolkit. Neural Regen. Res. *21*, 534–541. https://doi.org/10.4103/NRR.NRR-D-24-01013.

79. Yang, L., Kress, B.T., Weber, H.J., Thiyagarajan, M., Wang, B., Deane, R., Benveniste, H., Iliff, J.J., and Nedergaard, M. (2013). Evaluating glymphatic pathway function utilizing clinically relevant intrathecal infusion of CSF tracer. J. Transl. Med. *11*, 107. https://doi.org/10.1186/1479-5876-11-107.

80. Hablitz, L.M., Vinitsky, H.S., Sun, Q., Stæger, F.F., Sigurdsson, B., Mortensen, K.N., Lilius, T.O., and Nedergaard, M. (2019). Increased glymphatic influx is correlated with high EEG delta power and low heart rate in mice under anesthesia. Sci. Adv. *5*, eaav5447. https://doi.org/10.1126/sciadv.aav5447.

81. Ruhland, M.K., Roberts, E.W., Cai, E., Mujal, A.M., Marchuk, K., Beppler, C., Nam, D., Serwas, N.K., Binnewies, M., and Krummel, M.F. (2020). Visualizing Synaptic Transfer of Tumor Antigens among Dendritic Cells. Cancer Cell *37*, 786–799.e5. https://doi.org/10.1016/j.ccell.2020.05.002.

82. Nakamura, Y., Ishii, J., and Kondo, A. (2013). Bright fluorescence monitoring system utilizing Zoanthus sp. green fluorescent protein (ZsGreen) for human G-protein-coupled receptor signaling in microbial yeast cells. PLoS One *8*, e82237. https://doi.org/10.1371/journal.pone.0082237.

83. Roberts, E.W., Broz, M.L., Binnewies, M., Headley, M.B., Nelson, A.E., Wolf, D.M., Kaisho, T., Bogunovic, D., Bhardwaj, N., and Krummel, M.F. (2016). Critical Role for CD103(+)/CD141(+) Dendritic Cells Bearing CCR7 for Tumor Antigen Trafficking and Priming of T Cell Immunity in Melanoma. Cancer Cell *30*, 324–336. https://doi.org/10.1016/j.ccell.2016.06.003.

84. Kersten, K., You, R., Liang, S., Tharp, K.M., Pollack, J., Weaver, V.M., Krummel, M.F., and Headley, M.B. (2023). Uptake of tumor-derived microparticles induces metabolic reprogramming of macrophages in the early metastatic lung. Cell Rep. *42*, 112582. https://doi.org/10.1016/j.celrep.2023.112582.

85. Yi, R., Chen, E., Roberts, E.W., Krummel, M.F., and Serwas, N.K. (2022). Impact of protein identity on tumor-associated antigen uptake into infiltrating immune cells: A comparison of different fluorescent proteins as

model antigens. PLoS One *17*, e0272857. https://doi.org/10.1371/journal.pone.0272857.

86. Szatanek, R., Baran, J., Siedlar, M., and Baj-Krzyworzeka, M. (2015). Isolation of extracellular vesicles: Determining the correct approach (Review). Int. J. Mol. Med. *36*, 11–17. https://doi.org/10.3892/ijmm.2015.2194.

87. Matamoros-Angles, A., Karadjuzovic, E., Mohammadi, B., Song, F., Brenna, S., Meister, S.C., Siebels, B., Voß, H., Seuring, C., Ferrer, I., et al. (2024). Efficient enzyme-free isolation of brain-derived extracellular vesicles. J. Extracell. Vesicles *13*, e70011. https://doi.org/10.1002/jev2.70011.

88. Mestre, H., Hablitz, L.M., Xavier, A.L., Feng, W., Zou, W., Pu, T., Monai, H., Murlidharan, G., Castellanos Rivera, R.M., Simon, M.J., et al. (2018). Aquaporin-4-dependent glymphatic solute transport in the rodent brain. eLife *7*, e40070. https://doi.org/10.7554/eLife.40070.

89. Smyth, L.C.D., Xu, D., Okar, S.V., Dykstra, T., Rustenhoven, J., Papadopoulos, Z., Bhasiin, K., Kim, M.W., Drieu, A., Mamuladze, T., et al. (2024). Identification of direct connections between the dura and the brain. Nature *627*, 165–173. https://doi.org/10.1038/s41586-023-06993-7.

90. Yang, A.C., du Bois, H., Olsson, N., Gate, D., Lehallier, B., Berdnik, D., Brewer, K.D., Bertozzi, C.R., Elias, J.E., and Wyss-Coray, T. (2018). Multiple Click-Selective tRNA Synthetases Expand Mammalian Cell-Specific Proteomics. J. Am. Chem. Soc. *140*, 7046–7051. https://doi.org/10.1021/jacs.8b03074.

91. Pietilä, R., Del Gaudio, F., He, L., Vázquez-Liébanas, E., Vanlandewijck, M., Muhl, L., Mocci, G., Bjørnholm, K.D., Lindblad, C., Fletcher-Sandersjöö, A., et al. (2023). Molecular anatomy of adult mouse leptomeninges. Neuron *111*, 3745–3764.e7. https://doi.org/10.1016/j.neuron.2023.09.002.

92. DeSisto, J., O'Rourke, R., Jones, H.E., Pawlikowski, B., Malek, A.D., Bonney, S., Guimiot, F., Jones, K.L., and Siegenthaler, J.A. (2020). Single-Cell Transcriptomic Analyses of the Developing Meninges Reveal Meningeal Fibroblast Diversity and Function. Dev. Cell *54*, 43–59.e4. https://doi.org/10.1016/j.devcel.2020.06.009.

93. Van Hove, H., Martens, L., Scheyltjens, I., De Vlaminck, K., Pombo Antunes, A.R., De Prijck, S., Vandamme, N., De Schepper, S., Van Isterdael, G., Scott, C.L., et al. (2019). A single-cell atlas of mouse brain macrophages reveals unique transcriptional identities shaped by ontogeny and tissue environment. Nat. Neurosci. *22*, 1021–1035. https://doi.org/10.1038/s41593-019-0393-4.

94. Rustenhoven, J., and Kipnis, J. (2022). Brain borders at the central stage of neuroimmunology. Nature *612*, 417–429. https://doi.org/10.1038/s41586-022-05474-7.

95. Wang, Y., Chen, D., Xu, D., Huang, C., Xing, R., He, D., and Xu, H. (2021). Early developing B cells undergo negative selection by central nervous system-specific antigens in the meninges. Immunity *54*, 2784–2794.e6. https://doi.org/10.1016/j.immuni.2021.09.016.

96. Schafflick, D., Wolbert, J., Heming, M., Thomas, C., Hartlehnert, M., Börsch, A.L., Ricci, A., Martín-Salamanca, S., Li, X., Lu, I.N., et al. (2021). Single-cell profiling of CNS border compartment leukocytes reveals that B cells and their progenitors reside in non-diseased meninges. Nat. Neurosci. *24*, 1225–1234. https://doi.org/10.1038/s41593-021-00880-y.

97. Yang, S.Y., Long, J., Huang, M.X., Luo, P.Y., Bian, Z.H., Xu, Y.F., Wang, C.B., Yang, S.H., Li, L., Selmi, C., et al. (2021). Characterization of Organ-Specific Regulatory B Cells Using Single-Cell RNA Sequencing. Front. Immunol. *12*, 711980. https://doi.org/10.3389/fimmu.2021.711980.

98. Graybuck, L.T., Daigle, T.L., Sedeño-Cortés, A.E., Walker, M., Kalmbach, B., Lenz, G.H., Morin, E., Nguyen, T.N., Garren, E., Bendrick, J.L., et al. (2021). Enhancer viruses for combinatorial cell-subclass-specific labeling. Neuron *109*, 1449–1464.e13. https://doi.org/10.1016/j.neuron.2021.03.011.

99. Hunker, A.C., Wirthlin, M.E., Gill, G., Johansen, N.J., Hooper, M., Omstead, V., Vargas, S., Lerma, M.N., Taskin, N., Weed, N., et al. (2025). Enhancer AAV toolbox for accessing and perturbing striatal cell types and circuits. Neuron *113*, 1507–1524.e17. https://doi.org/10.1016/j.neuron.2025.04.035.

100. Oakley, H., Cole, S.L., Logan, S., Maus, E., Shao, P., Craft, J., Guillozet-Bongaarts, A., Ohno, M., Disterhoft, J., Van Eldik, L., et al. (2006). Intraneuronal beta-amyloid aggregates, neurodegeneration, and neuron loss in transgenic mice with five familial Alzheimer's disease mutations: potential factors in amyloid plaque formation. J. Neurosci. *26*, 10129–10140. https://doi.org/10.1523/JNEUROSCI.1202-06.2006.

101. Banks, W.A., Gray, A.M., Erickson, M.A., Salameh, T.S., Damodarasamy, M., Sheibani, N., Meabon, J.S., Wing, E.E., Morofuji, Y., Cook, D.G., et al. (2015). Lipopolysaccharide-induced blood-brain barrier disruption: Roles of cyclooxygenase, oxidative stress, neuroinflammation, and elements of the neurovascular unit. J. Neuroinflamm. *12*, 223. https://doi.org/10.1186/s12974-015-0434-1.

102. Zhao, J., Bi, W., Xiao, S., Lan, X., Cheng, X., Zhang, J., Lu, D., Wei, W., Wang, Y., Li, H., et al. (2019). Neuroinflammation induced by lipopolysaccharide causes cognitive impairment in mice. Sci. Rep. *9*, 5790. https://doi.org/10.1038/s41598-019-42286-8.

103. Smyth, L.C.D., Verhaege, D., Standen-Bloom, E., Wu, Y., Gan, Y., Storck, S.E., Boskovic, P., Plog, B.A., Mamuladze, T., Mazzitelli, J.A., et al. (2026). Amyloidosis of bridging veins is a pathologic feature of Alzheimer's disease. J. Exp. Med. *223*, e20251860. https://doi.org/10.1084/jem.20251860.

104. Xue, Y., Liu, X., Koundal, S., Constantinou, S., Dai, F., Santambrogio, L., Lee, H., and Benveniste, H. (2020). In vivo T1 mapping for quantifying glymphatic system transport and cervical lymph node drainage. Sci. Rep. *10*, 14592. https://doi.org/10.1038/s41598-020-71582-x.

105. Sarker, A., Suh, M., Choi, Y., Park, J.Y., Lee, Y.S., and Lee, D.S. (2023). Intrathecal [(64)Cu]Cu-albumin PET reveals age-related decline of lymphatic drainage of cerebrospinal fluid. Sci. Rep. *13*, 12930. https://doi.org/10.1038/s41598-023-39903-y.

106. Kim, M.W., Gao, W., Lichti, C.F., Gu, X., Dykstra, T., Cao, J., Smirnov, I., Boskovic, P., Kleverov, D., Salvador, A.F.M., et al. (2025). Endogenous self-peptides guard immune privilege of the central nervous system. Nature *637*, 176–183. https://doi.org/10.1038/s41586-024-08279-y.

107. Rakic, P. (2009). Evolution of the neocortex: a perspective from developmental biology. Nat. Rev. Neurosci. *10*, 724–735. https://doi.org/10.1038/nrn2719.

108. Buckner, R.L., and Krienen, F.M. (2013). The evolution of distributed association networks in the human brain. Trends Cogn. Sci. *17*, 648–665. https://doi.org/10.1016/j.tics.2013.09.017.

109. Ringstad, G., and Eide, P.K. (2020). Cerebrospinal fluid tracer efflux to parasagittal dura in humans. Nat. Commun. *11*, 354. https://doi.org/10.1038/s41467-019-14195-x.

110. Absinta, M., Ha, S.K., Nair, G., Sati, P., Luciano, N.J., Palisoc, M., Louveau, A., Zaghloul, K.A., Pittaluga, S., Kipnis, J., et al. (2017). Human and nonhuman primate meninges harbor lymphatic vessels that can be visualized noninvasively by MRI. eLife *6*, e29738. https://doi.org/10.7554/eLife.29738.

111. Mrdjen, D., Pavlovic, A., Hartmann, F.J., Schreiner, B., Utz, S.G., Leung, B.P., Lelios, I., Heppner, F.L., Kipnis, J., Merkler, D., et al. (2018). High-Dimensional Single-Cell Mapping of Central Nervous System Immune Cells Reveals Distinct Myeloid Subsets in Health, Aging, and Disease. Immunity *48*, 599. https://doi.org/10.1016/j.immuni.2018.02.014.

112. Vara-Pérez, M., and Movahedi, K. (2025). Border-associated macrophages as gatekeepers of brain homeostasis and immunity. Immunity *58*, 1085–1100. https://doi.org/10.1016/j.immuni.2025.04.005.

113. Kierdorf, K., Masuda, T., Jordão, M.J.C., and Prinz, M. (2019). Macrophages at CNS interfaces: ontogeny and function in health and disease. Nat. Rev. Neurosci. *20*, 547–562. https://doi.org/10.1038/s41583-019-0201-x.

114. Min, H., O'Neil, S.M., Xu, L., Moseman, E.A., Kurtzberg, J., and Filiano, A.J. (2024). Mural cells interact with macrophages in the dura mater to regulate CNS immune surveillance. J. Exp. Med. *221*, e20230326. https://doi.org/10.1084/jem.20230326.

115. Yang, M., Rui, K., Wang, S., and Lu, L. (2013). Regulatory B cells in autoimmune diseases. Cell. Mol. Immunol. *10*, 122–132. https://doi.org/10.1038/cmi.2012.60.

116. Liu, L., Zhang, X., Chai, Y., Zhang, J., Deng, Q., and Chen, X. (2025). Skull bone marrow and skull meninges channels: redefining the landscape of central nervous system immune surveillance. Cell Death Dis. *16*, 53. https://doi.org/10.1038/s41419-025-07336-2.

117. Eme-Scolan, E., Gomes, M., Bani, A., Romano, A., Kassem, O., Roussel-Queval, A., Casel, B., Slimani, L., Lawrence, T., and Rua, R. (2026). Remodeling of skull bone channels regulates immune infiltration into the meninges during neuroinflammation. Immunity *59*, 116–128.e7. https://doi.org/10.1016/j.immuni.2025.11.019.

118. Rustenhoven, J., Pavlou, G., Storck, S.E., Dykstra, T., Du, S., Wan, Z., Quintero, D., Scallan, J.P., Smirnov, I., Kamm, R.D., et al. (2023). Age-related alterations in meningeal immunity drive impaired CNS lymphatic drainage. J. Exp. Med. *220*, e20221929. https://doi.org/10.1084/jem.20221929.

119. Plog, B.A., Dashnaw, M.L., Hitomi, E., Peng, W., Liao, Y., Lou, N., Deane, R., and Nedergaard, M. (2015). Biomarkers of traumatic injury are transported from brain to blood via the glymphatic system. J. Neurosci. *35*, 518–526. https://doi.org/10.1523/JNEUROSCI.3742-14.2015.

120. Arbel-Ornath, M., Hudry, E., Eikermann-Haerter, K., Hou, S., Gregory, J.L., Zhao, L., Betensky, R.A., Frosch, M.P., Greenberg, S.M., and Bacskai, B.J. (2013). Interstitial fluid drainage is impaired in ischemic stroke and Alzheimer's disease mouse models. Acta Neuropathol. *126*, 353–364. https://doi.org/10.1007/s00401-013-1145-2.

121. Guldner, I.H., Wagner, V.P., Moran-Losada, P., Shi, S.M., Golub, S.W., Hevler, J.F., Chen, K., Meese, B.T., Ghoochani, A., Pulido, E., et al. (2026). Ageing promotes microglial accumulation of slow-degrading synaptic proteins. Nature *650*, 930–941. https://doi.org/10.1038/s41586-025-09987-9.

122. Roussel-Queval, A., Rebejac, J., Eme-Scolan, E., Paroutaud, L.A., and Rua, R. (2023). Flow cytometry and immunohistochemistry of the mouse dural meninges for immunological and virological assessments. STAR Protoc. *4*, 102119. https://doi.org/10.1016/j.xpro.2023.102119.

123. Upadhyay, A., Chhangani, D., Rao, N.R., Kofler, J., Vassar, R., Rincon-Limas, D.E., and Savas, J.N. (2023). Amyloid fibril proteomics of AD brains reveals modifiers of aggregation and toxicity. Mol. Neurodegener. *18*, 61. https://doi.org/10.1186/s13024-023-00654-z.

124. Stuart, T., Butler, A., Hoffman, P., Hafemeister, C., Papalexi, E., Mauck, W.M., 3rd, Hao, Y., Stoeckius, M., Smibert, P., and Satija, R. (2019). Comprehensive Integration of Single-Cell Data. Cell *177*, 1888–1902.e21. https://doi.org/10.1016/j.cell.2019.05.031.

125. Satija, R., Farrell, J.A., Gennert, D., Schier, A.F., and Regev, A. (2015). Spatial reconstruction of single-cell gene expression data. Nat. Biotechnol. *33*, 495–502. https://doi.org/10.1038/nbt.3192.

126. Hao, Y., Stuart, T., Kowalski, M.H., Choudhary, S., Hoffman, P., Hartman, A., Srivastava, A., Molla, G., Madad, S., Fernandez-Granda, C., et al. (2024). Dictionary learning for integrative, multimodal and scalable single-cell analysis. Nat. Biotechnol. *42*, 293–304. https://doi.org/10.1038/s41587-023-01767-y.

127. McGinnis, C.S., Murrow, L.M., and Gartner, Z.J. (2019). DoubletFinder: Doublet Detection in Single-Cell RNA Sequencing Data Using Artificial Nearest Neighbors. Cell Syst. *8*, 329–337.e4. https://doi.org/10.1016/j.cels.2019.03.003.

128. Korsunsky, I., Millard, N., Fan, J., Slowikowski, K., Zhang, F., Wei, K., Baglaenko, Y., Brenner, M., Loh, P.R., and Raychaudhuri, S. (2019). Fast, sensitive and accurate integration of single-cell data with Harmony. Nat. Methods *16*, 1289–1296. https://doi.org/10.1038/s41592-019-0619-0.

129. Kim, M.C., Gate, R., Lee, D.S., Tolopko, A., Lu, A., Gordon, E., Shifrut, E., Garcia-Nieto, P.E., Marson, A., Ntranos, V., et al. (2024). Method of moments framework for differential expression analysis of single-cell RNA sequencing data. Cell *187*, 6393–6410.e16. https://doi.org/10.1016/j.cell.2024.09.044.

130. Levine, J.H., Simonds, E.F., Bendall, S.C., Davis, K.L., Amir, E., Tadmor, M.D., Litvin, O., Fienberg, H.G., Jager, A., Zunder, E.R., et al. (2015). Data-Driven Phenotypic Dissection of AML Reveals Progenitor-like Cells that Correlate with Prognosis. Cell *162*, 184–197. https://doi.org/10.1016/j.cell.2015.05.047.

131. Cao, J., Packer, J.S., Ramani, V., Cusanovich, D.A., Huynh, C., Daza, R., Qiu, X., Lee, C., Furlan, S.N., Steemers, F.J., et al. (2017). Comprehensive single-cell transcriptional profiling of a multicellular organism. Science *357*, 661–667. https://doi.org/10.1126/science.aam8940.

132. Trapnell, C., Cacchiarelli, D., Grimsby, J., Pokharel, P., Li, S., Morse, M., Lennon, N.J., Livak, K.J., Mikkelsen, T.S., and Rinn, J.L. (2014). The dynamics and regulators of cell fate decisions are revealed by pseudotemporal ordering of single cells. Nat. Biotechnol. *32*, 381–386. https://doi.org/10.1038/nbt.2859.

Please cite this article in press as: Chayama et al., Physiological brain clearance architecture revealed by neuronal protein tracing, Cell (2026), https://doi.org/10.1016/j.cell.2026.04.048

STAR★METHODS

KEY RESOURCES TABLE

REAGENT or RESOURCE	SOURCE	IDENTIFIER
Antibodies		
NeuN	Abcam	Cat#ab177487; RRID:AB_2532109
Cre recombinase	Cell Systems Technologies	Cat#15036S; RRID:AB_2798694
GFAP	Thermo Fisher Scientific	Cat#50-173-4108
Iba1	Wako	Cat#019-19741; RRID:AB_839504
CD31 (PECAM-1)	R&D Systems	Cat#AF3628; RRID:AB_2161028
CD206	Thermo Fisher Scientific	Cat#MA5-16868; RRID:AB_2538346
ACSA-2	Miltenyi Biotec	Cat#130-116-243
TSG101	Santa Cruz Biotechnology	Cat#sc-7964; RRID:AB_671392
Aβ42	Santa Cruz Biotechnology	Cat#sc-28365; RRID:AB_626669
CD274 (PD-L1)	Santa Cruz Biotechnology	Cat#sc-28365; RRID:AB_467781
CD11b	BioLegend	Cat#101257; RRID:AB_2561373
Ly6C	BioLegend	Cat#128026; RRID:AB_10640120
LYVE-1	AngioBio	Cat#11-034; RRID:AB_2813732
CD81	Santa Cruz Biotechnology	Cat#sc-166029; RRID:AB_2275892
B220	Thermo Fisher Scientific	Cat#19-0452-82; RRID:AB_467254
Bacterial and virus strains		
AAV-PHP.eB-hSyn-Cre.WPRE.hGH	James M. Wilson; Addgene	Addgene plasmid #105553; RRID:Addgene_105553
AiP14825: pAAV-AiE0441h_3xC2-minBG-iCre(R297T)-BGHpA (Alias: CN4825), AAV-PHP.eB viral prep	Allen Institute for Brain Science & Jonathan Ting; Addgene	Addgene viral prep #214862-PHPeB; RRID:Addgene_214862
AiP11851: pAAV-hDLX-minBG-iCre-4X2C-WPRE3-BGHpA (Alias: CN1851) viral prep	Addgene	Addgene viral prep #164450-PHPeB; RRID:Addgene_164450
AAV-PHP.eB-hSyn-ZsGreen-P2A-mCherry-NLS-SV40	This paper	N/A
Chemicals, peptides, and recombinant proteins		
Alexa Fluor-conjugated ovalbumin	Thermo Fisher Scientific	Cat# O34784; O34782
g4-azido-L-phenylalanine (AzF)	Vector Laboratories	Cat#1406-5G
DBCO-Alexa Fluor 647	Vector Laboratories	CCT-1302-1
Cadaverine-Alexa Fluor 647	Invitrogen	Cat#A30677
CUBIC-L	TCI	Cat#T3740
CUBIC-R+(N)	TCI	Cat#T3983
EasyIndex Matched Immersion Oil (RI:1.52)	LifeCanvas Technologies	Cat#Oil-1.52
Lipopolysaccharide (LPS)	Sigma-Aldrich	L2880A
WGA-647	Fisher Scientific	Cat# W32466
Copper (II) sulfate ($CuSO_4$)	Sigma-Aldrich	Cat# 451657-10G
THPTA	Vector Laboratories	Cat# 1010-500
Aminoguanidine hydrochloride	Sigma-Aldrich	Cat# 396494-25G
Sodium ascorbate (sodium L-ascorbate)	TCI	Cat# A0539-25G
Iodoacetamide (IAA)	Sigma-Aldrich	Cat# I1149-25G
LDS Sample Buffer	Invitrogen	Cat# NP0008
Critical commercial assays		
BCA Protein Assay Kit	Thermo Scientific	Cat#23225
Neural Tissue Dissociation Kit	Miltenyi Biotec	Cat#130-092-628

(*Continued on next page*)

Please cite this article in press as: Chayama et al., Physiological brain clearance architecture revealed by neuronal protein tracing, Cell (2026), https://doi.org/10.1016/j.cell.2026.04.048

Continued

REAGENT or RESOURCE	SOURCE	IDENTIFIER
GEM-X Flex Sample Preparation v2 Kit	10x Genomics	Cat#PN-1000781
Feature Barcoding Multiplexing Kit	10x Genomics	N/A
Experimental models: Organisms/strains		
C57BL/6J	The Jackson Laboratory	RRID:IMSR_JAX:000664
ZsGreen	The Jackson Laboratory	RRID:IMSR_JAX:007906
5XFAD	The Jackson Laboratory	RRID:MMRRC_034840-JAX
CaMKII-Cre	The Jackson Laboratory	RRID:IMSR_JAX:005359
PheRS	The Jackson Laboratory	RRID:IMSR_JAX:033734
Forebrain-ZsG: CaMKII-Cre x ZsGreen	This paper	N/A
Oligonucleotides		
Primers and labeled probes targeting AAV ITR sequence for qPCR titering	This paper	N/A
Custom 10x Genomics probe set targeting Cre recombinase	This paper	N/A
Custom 10x Genomics probe set targeting ZsGreen	This paper	N/A
Software and algorithms		
Imaris v10.2.1	Oxford Instruments	https://imaris.oxinst.com/
FlowJo	FlowJo, LLC / BD Biosciences	https://www.flowjo.com/
Cell Ranger	10x Genomics	https://www.10xgenomics.com/support/software/cell-ranger/latest
R (v4.5.1)	R Foundation for Statistical Computing	https://www.r-project.org/ (RRID:SCR_001905)
Seurat v5.2.1	Satija Lab	https://satijalab.org/seurat/ (RRID:SCR_016341)
DoubletFinder (v 2.0.4)	McGinnis & Gartner Lab	https://github.com/chris-mcginnis-ucsf/DoubletFinder (RRID:SCR_018771)
Harmony (v 1.2.3)	Raychaudhuri Lab	https://github.com/immunogenomics/harmony (RRID:SCR_022206)
Memento v0.1.5	Ye Lab	https://memento.readthedocs.io/
Monocle3 (v1.4.26)	Cole Trapnell Lab	https://cole-trapnell-lab.github.io/monocle3/ (RRID:SCR_018685)
Python (v 3.12.0)	Python Software Foundation	https://www.python.org/downloads/source/ (RRID:SCR_008394)
Scanpy (v 1.10.4)	Theis Lab	https://scanpy.readthedocs.io/en/stable/ (RRID:SCR_018139)
Numpy (v 1.26.4)	NumPy Community	https://numpy.org/ (RRID:SCR_008633)
Pandas (v 2.3.3)	pandas Development Team	https://pandas.pydata.org/ (RRID:SCR_018214)
Other		
Stereotaxic frame (Model 940)	Kopf Instruments	Model 940
Hamilton syringe	Hamilton Company	N/A
33G/31G needle	VWR	N/A
Insulin syringe	Fisher Scientific	Cat# 22-024-306
Osmotic pump (Model 2002; 0.50 μL/hr)	Alzet	Cat#0000296
Brain infusion cannula kit 3 (for ICV infusion)	Alzet	Cat#0008851
0.5 mm microburr	Fine Science Tools	Cat#19007-05

Please cite this article in press as: Chayama et al., Physiological brain clearance architecture revealed by neuronal protein tracing, Cell (2026), https://doi.org/10.1016/j.cell.2026.04.048

EXPERIMENTAL MODEL AND STUDY PARTICIPANT DETAILS

Animals

C57BL/6J (RRID:IMSR_JAX:000664), ZsGreen (IMSR_JAX:007906), 5XFAD (RRID:MMRRC_034840-JAX), CaMKII-Cre (RRID:IMSR_JAX:005359), and PheRS (RRID:IMSR_JAX:033734) mice were obtained from Jackson Laboratory and bred in-house. For Forebrain-ZsG mice, ZsGreen mice were crossed and bred in house to CaMKII-Cre mice to achieve homozygous robust ZsGreen expression in CaMKII-positive neurons. Young adult mice of both sexes under the written age are used. All animals were fed ad libitum and housed under 12-hour light/dark cycles (7 a.m. - 7 p.m.), under the control of humidity and temperature. All experiments were approved by the Institutional Animal Care and Use Committee of the University of California, San Francisco (#AN206908-00A).

AAV Production

The pENN.AAV.hSyn.Cre.WPRE.hGH was a gift from James M. Wilson (Addgene plasmid # 105553, RRID:Addgene 105553) and was packaged to AAV-PHPeB in house or in VectorBuilder for bulk production. The AiP14825: pAAV-AiE0441h_3xC2-minBG-iCre(R297T)-BGHpA (Alias: CN4825) was a gift from The Allen Institute for Brain Science & Jonathan Ting (Addgene viral prep # 214862-PHPeB; RRID:Addgene 214862).[99] The viral prep of AiP11851-pAAV-hDLX-minBG-iCre-4X2C-WPRE3-BGHpA (Alias: CN1851) was purchased through Addgene.[98] AAV was otherwise produced in-house using HEK293T cells as the packaging cell line. Cells were maintained in Dulbecco's Modified Eagle Medium (DMEM) supplemented with 10% fetal bovine serum (FBS), 100 U/mL penicillin, and 100 μg/mL streptomycin at 37°C in a humidified incubator with 5% CO_2. For transfection, cells were plated at 30-40% confluence in 15 cm dishes 24 hours prior, reaching 70-80% confluence at the time of transfection. DNA was transfected using a polyethyleneimine (PEI)-based method with modifications. Cells were incubated at 37°C for 3 days post-transfection before harvesting. They were then lysed by three freeze-thaw cycles. The lysate was filtered through a .45μm PES filter, and AAV particles were precipitated using differential-speed ultracentrifugation. Vector titers were determined by quantitative PCR (qPCR) using primers and labeled probes targeting the ITR sequence.

Retroorbital Injection

Male and female mice received retro-orbital injections of AAV vectors capable of crossing the blood-brain barrier. Mice were anesthetized with 2-3% isoflurane prior to the procedure. The virus was diluted to a concentration of approximately 6-8 $\times$ 10^{12} genome copies (GC) per mL in sterile saline. A total volume of 100 μL (equivalent to 6-8 $\times$ 10^{11} GC per mouse) was injected into the retro-orbital sinus of the right eye using a 31G needle attached to an insulin. After injection, mice were monitored and maintained for a 1-2 week expression period prior to sample collection.

Intracisterna magna (ICM) injections of tracers

Mice were anesthetized with 3.0-3.5% isoflurane and administered subcutaneous injections of buprenorphine and bupivacaine prior to surgery. The back of the neck was shaved and disinfected, and the mouse was positioned on a surgical stage to optimize alignment for access to the cisterna magna, as previously described. A midline incision was made, and the neck muscles were gently retracted to expose the cisterna magna. A total of 5 μL of Alexa Fluor-conjugated ovalbumin (8 mg/mL in PBS, Thermo Fischer product# O34782) was injected at a rate of 1 μL/min using a Hamilton syringe connected to a 33G needle via silicone tubing. Following the injection, the needle was held in place with positive pressure for 2 minutes to prevent backflow. The incision site was closed using a surgical stapler, and mice were placed on a heating pad until fully recovered. Meloxicam was administered subcutaneously immediately after surgery.

Intrastriatal injection of OVA

Mice were anesthetized with isoflurane before being placed in a stereotaxic injection rig. Mouse head was restrained by ear bars with placing the front teeth in the holding apparatus. Isoflurane and oxygen were provided at a low flow rate to keep the mouse anesthetized during the whole procedure. To prevent from drying, the eyeballs were covered with ophthalmic ointment. Buprenex (0.1 mg/kg) was administrated by intraperitoneal injection. 5μL of Alexa Fluor-conjugated ovalbumin (8 mg/mL in PBS) were injected in each striatum using Hamilton needles. Injection sites, ±1.8 mediolateral, 0.74 anteroposterior, and −3.5 dorsoventral. An automatic injection pump was used to control the speed at 200 nl/min. The needle was holding at injection position for 10 min before slow withdrawal. After closing the wound, meloxicam (1 mg/kg) was administrated by intraperitoneal injection. The mouse was put onto a warming pad for recovery.

Chronic CSF-infusion of OVA

For intracerebroventricular infusions, osmotic pumps (Alzet Model 2002, 0.50 μL/hr, Cat #0000296) were filled with OVA-647 (diluted to delivery 40μg/day) and connected to brain infusion cannulas (Alzet brain infusion kit 3, Cat. 0008851) modified with a spacer disc to enable ventricular targeting. Mice were anesthetized with isoflurane (Dechra, Cat. #200-129) and secured in a stereotaxic frame (Kopf Instruments Model 940). The scalp was shaved, and a midline incision was made to expose the skull. After identifying bregma, a stereotaxic site was drilled with a 0.5 mm microburr (Fine Science Tools, Cat. #19007-05) at coordinates X = +1.0 mm and Y = −0.25mm. Osmotic pump was implanted in a subcutaneous pocket formed on the back of the mouse, and the connected infusion cannula was

Please cite this article in press as: Chayama et al., Physiological brain clearance architecture revealed by neuronal protein tracing, Cell (2026), https://doi.org/10.1016/j.cell.2026.04.048

inserted Z = -2.0mm through the drill site and into the right lateral ventricle. The incision was closed with nylon monofilament non-absorbable 6-0 sutures (Surgical Specialties Look, Cat. #911B). Lidocaine (Vedco) was applied subcutaneously along the incision, and buprenorphine (Henry Schein, Cat. #55175) and ketofen (Henry Schein, Cat. #005487) were administered for analgesia. Mice were monitored on a heating pad until ambulatory and then single-housed for 14 days before collection.

Endogenous labeling of neuronal proteomes

To generate Syn-PheRS mice, PHP.eB.hSyn.Cre.WPRE.hGH AAV was RO injected into PheRS mice and let to transduce for 8-10 days. Following transduction, 185mg/kg of g4-azido-l-phenylalanine (Vector Laboratories; 1406-5G AzF) was intraperitoneally administered to Syn-PheRS mice every day for one week.[121] For pulse-chase kinetic experiments, after Syn-PheRS received one week of labeling, wash out periods of 2 and 5 days where AzF was withdrawn. Mice were collected at T0, T2, and T5 timepoints for downstream analyses.

METHOD DETAILS

Cu-Click for IHC

Tissue sections were processed for click chemistry labeling of azide-modified proteins following the standard immunofluorescence protocol through the blocking step. Sections were then incubated for 1 h in a CuAAC reaction containing Alexa Fluor 647-alkyne (5 mM), $CuSO_4$ (20 mM), THPTA (50 mM), aminoguanidine hydrochloride (50 mM), sodium l-ascorbate (50 mM), and PBS. $CuSO_4$ and THPTA were pre-complexed at a 1:2 ratio for 15 min prior to addition of the remaining reagents. After the reaction, sections were washed three times in TBS-T and either subjected to subsequent immunofluorescence staining or mounted and cover slipped.

In-gel fluorescence detection of azide-modified proteins

For detection and quantitation of azide-modified proteins across brain border homogenates from Syn-PheRS mice, we utilized DBCO-based click chemistry. Protein lysates (250–500 μg per tissue) were reduced with 10 mM dithiothreitol (DTT) for 10-15 min at room temperature, followed by alkylation with 20 mM iodoacetamide (IAA) for 20 min in the dark. Excess IAA was quenched by the addition of DTT to a final concentration of 20 mM and incubated for 15 min at room temperature. Samples were then incubated with 6 μM DBCO-Alexa Fluor 647 (Click Chemistry Tools) for 1 h at room temperature with rotation in the dark. Following labeling, samples were mixed with LDS sample buffer and boiled for 10 min. Labeled homogenates were then run by SDS-PAGE.

Immunohistochemistry

Mice were anesthetized via intraperitoneal injection of Avertin solution. Brains, dura, skulls, and lymph nodes were collected following transcardial perfusion with cold PBS. Brains were post-fixed in 4% paraformaldehyde (PFA) in PBS overnight at 4°C, then cryoprotected in 30% sucrose/PBS for at least two overnights. Brains were sectioned at 40μm thickness using a microtome (Leica), and sections were stored in cryoprotectant solution at –20°C until immunostaining. Before staining, brain sections were washed three times in TBS with 0.1% Tween-20 (TBST, Sigma-Aldrich) to remove the cryoprotectant, then blocked and permeabilized in blocking buffer (2% normal donkey serum, 0.2% Triton X-100 in TBS) for 30 minutes with shake at room temperature.

Dura and skulls were fixed in 4% PFA/PBS for 3 days. The dorsal dura was carefully dissected from the skull cap and processed immediately without storage. Tissues were washed three times in TBST and then blocked and permeabilized in the blocking buffer for 30 minutes at room temperature.

Skulls were decalcified in 0.5M EDTA for more than 5 days, cryoprotected in 30% sucrose/PBS for 1-2 days, and embedded in OCT compound. The OCT-embedded samples were stored at –80°C until sectioning. Cryosections of skull tissue (20 μm) were collected on adhesive glass slides (SuperFrost Plus, Fisher Scientific), air-dried, and stored at –80°C until immunostaining.

Fresh lymph nodes were embedded in OCT compound immediately after collection from perfused animals, frozen on dry ice, and stored at –80°C. Cryosections (20 μm thickness) were placed on adhesive glass slides and stored at –80°C until immunostaining.

For immunostaining, the primary antibodies were applied at a 1:100-1000 dilution in blocking buffer and incubated overnight at 4 °C After three washes with TBST, appropriate fluorophore-conjugated secondary antibodies (1:200 dilution) were applied and incubated overnight at 4 °C. Sections were then washed again with TBST and mounted on glass slides using VectaShield mounting medium (H1800 or H1700). Images were acquired using confocal microscopes (LSM880 and LSM700).

Tissue Clearing and Light Sheet Fluorescence Imaging

Mice were anesthetized via intraperitoneal injection of Avertin solution, euthanized by severing the right atrium to allow exsanguination, and then intracardially perfused with 50–80 mL of cold PBS to flush out blood, followed by 35 mL of Alexa Fluor–conjugated wheat germ agglutinin (10 μg/mL in PBS) to label blood vessels, and finally 40 mL of 4% paraformaldehyde (PFA) in PBS for fixation. For whole-brain clearing, the brain was carefully extracted post-perfusion and incubated in 4% PFA/PBS at 4 °C overnight, followed by the CUBIC tissue clearing protocol. For head clearing, the entire head was collected after perfusion, trimmed to remove skin and eyeballs while preserving the skull and surrounding tissues, including muscles, salivary glands, lymph nodes, and ligaments. The trimmed head was incubated in 4% PFA/PBS overnight at 4 °C, then decalcified in 0.5 M EDTA at 37 °C for 5–7 days. Following three PBS washes, the head was coronally bisected at the level of the bregma into anterior and posterior halves prior to CUBIC clearing. For

both brain and head samples, tissues were incubated in CUBIC-L (TCI, cat #T3740) at 37 °C for 5–7 days with agitation for delipidation. The CUBIC-L solution was refreshed periodically when it turned yellow during the process. After delipidation, tissues were washed three times in PBS, then sequentially immersed in 50% and 100% CUBIC-R+(N) (TCI, cat# T3983) for refractive index (RI) matching. For skull imaging (head samples without brain), the head was sagittally halved after EDTA decalcification, and the brain was gently removed. The skull was delipidated in CUBIC-L at 37 °C for 5–7 days with agitation, washed three times in PBS, and blocked/permeabilized overnight at room temperature in blocking buffer (2% normal donkey serum, 0.2% Triton X-100, 0.2% NaN_3 in TBS). Following three additional washes with TBST and three rinses with PBS, the samples were immersed in CUBIC-R+(N) for refractive index (RI) matching. Fluorescence 3D imaging was conducted using a light sheet fluorescence microscope (UltraMicroscope Blaze, Miltenyi) with EasyIndex Matched Immersion Oil (RI:1.52) (life canvas technologies, cat# Oil-1.52). Imaging was performed using 405, 488, 588, and 647 nm lasers, with a 1× objective lens and 1× zoom. Each optical plane was illuminated bilaterally from both the left and right sides. Tile scans were acquired and raw image files were converted to IMS format, stitched, and rendered into 3D reconstructions using Imaris software (Oxford Instrument, version10.2.1) for visualization and analysis.

Tissue homogenization and plate reader quantification

Mice were anesthetized via intraperitoneal injection of Avertin. Blood was collected from the right ventricle using an EDTA-coated syringe (25G, Fisher Scientific), transferred to a 1.5 mL protein low-binding tube, and centrifuged at 2,000 × g for 15 min at 4 °C to isolate plasma. Following blood collection, mice were perfused intracardially with cold PBS via the left ventricle. Tissues were dissected to remove muscle and connective tissue, segmented into defined anatomical regions, and transferred into individual tubes. Dorsal durae were carefully peeled from the dorsal skull. The basal skull and nasal cavity were further divided into subregions, including the nasal cavity, cribriform plate, lateral skull, and basal skull. All collected tissues were snap-frozen on dry ice and stored at −80 °C until further processing for protein extraction. Hard tissues (dorsal, lateral, and basal skulls, nasal cavity bone, and cribriform plate), along with the brain, were homogenized in RIPA lysis buffer supplemented with Halt protease inhibitor (Thermo Scientific), using metal beads (Revity) and a tissue homogenizer. Soft tissues (dura, sCLNs, and dCLNs) were homogenized using a probe sonicator. Homogenates were centrifuged at 15,000 × g for 15 min at 4 °C, and the supernatants were collected. Total protein concentrations were determined using the BCA Protein Assay Kit (Thermo Scientific). ZsGreen fluorescence was measured using 96-well fluorescence assay plates and a plate reader (Molecular Devices). The relative intensity values were calculated by normalizing fluorescence intensity to total protein concentration. To determine the fold enrichment of respective tracers at each border tissues were normalized to WT controls. For proportion of tracer at borders analyses, the border tracer levels were divided by the sum of tracer amounts across borders.

Western blot

For western blot analysis, protein concentrations in each sample were measured with BCA protein Assay Kit (Thermo Scientific). Equal quantities of protein samples were boiled for ten minutes in LDS buffer. Samples were then loaded onto the NU-PAGE precast gels and electrophoresed for high-resolution separation of proteins based on the size. Transfer onto 0.45-micron size nitrocellulose membrane was achieved in a Bio-Rad semi-dry quick transfer apparatus. Membrane blocking was done with 5% milk for 60 min before primary antibody incubation overnight at 4 °C. The next day, following four washes in TBST, five minutes each with shaking, membranes were probed with HRP-conjugated secondary antibodies obtained from the same host.

Flow cytometry

The brain, dura, skull, nasal cavity, and superficial and deep cervical lymph nodes (sCLNs and dCLNs, respectively) were collected in cold PBS or RPMI medium from mice, following intracardiac perfusion with cold PBS. Muscles and connective tissues were trimmed from the dorsal skull and nasal cavity bones. Brain cell suspensions were prepared using the Neural Tissue Dissociation Kit (Miltenyi Biotec, cat# 130-092-628), followed by myelin removal via centrifugation in 0.9 M sucrose/PBS. Dural cell suspensions were prepared according to a previously published protocol[122]: dorsal dura were peeled from the skull, pooled, and digested in an enzyme mix (2.5 mg/mL Collagenase D and 0.1 mg/mL DNase I in RPMI) at 37 °C for 30 minutes, followed by mechanical dissociation with 20-30 pipette strokes using a P1000 tip. Skull and nasal cavity cell suspensions were prepared following a previously described method.[62] Pooled tissues were minced in RPMI medium, vortexed at maximum speed for 30 seconds, and filtered through a 100 μm cell strainer. This process was repeated twice with fresh RPMI, and the resulting filtrates were pooled to generate a single cell suspension. Dissociated single-cell pellets were resuspended in cold PBS and passed through a 35 μm cell strainer of a FACS tube. From surface versus intracellular assays, dissociated cells were split in half and incubated in buffer with or without detergents. After centrifugation, cells were stained with Zombie NIR viability dye (BioLegend, cat#423106; 1:1000 dilution in PBS) on ice for 20 minutes. Following a wash with PBS, cells were blocked with Fc block (BD Biosciences, 1:100) and incubated on ice for 20 minutes with antibodies. After staining, cells were washed with FACS buffer, permeabilized (if needed) in IC buffer, fixed for 20 minutes, and stored in FACS buffer at 4 °C until analysis. For AzF detection, cells after FACs buffer and/or permeabilization were alkylated with 20mM IAA for 20 min in the dark before 1 hour incubation with 6μM DBCO-647. Flow cytometry was performed using a BD FACSAria Fusion (BD Biosciences). Acquired data was analyzed with FlowJo.

Please cite this article in press as: Chayama et al., Physiological brain clearance architecture revealed by neuronal protein tracing, Cell (2026), https://doi.org/10.1016/j.cell.2026.04.048

Single-Cell RNA Sequencing

Two weeks after AAV injection, the brain, dura, skull, and nasal cavity bone were collected in cold PBS or RPMI medium from Syn-ZsG mice (both sexes) following intracardiac perfusion with cold PBS. Single-cell suspensions from each tissue were prepared and stained using the same protocol as described for the flow cytometry experiments. To obtain sufficient cell numbers for sorting, tissues were pooled as follows: brain (n = 4), dorsal dura (n = 8), skull (n = 8), and nasal cavity bone (n = 4). Following antibody staining, cells were fixed overnight at 4 °C in Fixation Buffer from the GEM-X Flex Sample Preparation v2 Kit (10x Genomics, #PN-1000781). The next day, fixed cells were treated with Additive C (10x Genomics, #PN-1000781), centrifuged, and resuspended in PBS containing 1% nuclease-free BSA and 0.2 U/μL RNase inhibitor (Roche). Flow cytometry gating was performed to exclude debris (SSC-A vs. FSC-A), followed by selection of singlet cells (FSC-W vs. FSC-A), and gating of ZsGreen+ and - populations for sorting. Doublets and multiplets were excluded. Up to 50,000 to 100,000 cells were sorted per sample. Sorted cells were centrifuged and stored overnight at 4 °C prior to probe hybridization and GEM generation. Sorted cells were hybridized with probes (10x Genomics) according to the manufacturer's instructions. Custom probes targeting Cre recombinase and ZsGreen were designed following 10x Genomics guidelines. After hybridization, cells were loaded into the 10x Genomics Chromium system, and library preparation was performed using the GEM-X FLEX kit, following the manufacturer's protocol. Sequencing was conducted on an Illumina NovaSeq platform using paired-end reads in accordance with 10x Genomics recommendations.

Blood-Brain Barrier Permeability Assay

Mice were retro-orbitally injected under anesthesia using an insulin syringe (BD, 328421; 0.33 mm × 12.7 mm) with cadaverine-Alexa Fluor 647 (Invitrogen, A30677) at a concentration of 0.5 mg/mL, 100 μL per 20 g body weight. After a 2-hour circulation period, mice were perfused with 0.01 M PBS for 5 minutes, and brains were harvested for analysis. One hemisphere was weighed and homogenized in 1% Triton X-100 in 0.01 M PBS. The homogenate was centrifuged at 21,000 × g for 20 minutes at 4 °C, and the supernatant was collected.

LPS-induced inflammation

ZsGreen expression was allowed to develop for one-week. Mice then received an intraperitoneal injection of LPS (3 mg/kg) or PBS as a control. One day after LPS administration, tissues were collected for further analysis. Sample processing for protein quantification followed the same procedures described in the previous section.

5XFAD ZsGreen Induction

Neuronal ZsGreen expression was induced in 2- and 7-month-old 5XFAD and age-matched WT mice with retroorbital administration of 6×10^{11} GC PHPeB-hSyn-ZsGreen-P2A-mCherry-NLS-SV40. Transduction was allowed for 14 days before tissue collection and downstream analyses.

$A\beta_{42}$ ELISA

$A\beta_{42}$ ELISA analysis was performed as previously described,[123] in short homogenized tissues from brain, brain border tissues, and blood were diluted in the standard diluent buffer. 50μL of blank solution, standards, and samples were loaded into antibody-coated wells and incubated with detection antibody for 3hr at RT. After multiple washes, HRP-conjugated antibody was added for 30 min. After washes, the samples were incubated with stabilized chromogen for 30 min, and the reaction was stopped with an acid-based stop solution. OD was measured at 450 nm with plate reader (Molecular Devices) and compared to a standard curve to determine the final concentration.

QUANTIFICATION AND STATISTICAL ANALYSIS

scRNA-seq data preprocessing

Raw sequencing reads were aligned to a custom mm10 reference genome containing ZsGreen and Cre transgene sequences using Cell Ranger, and samples were demultiplexed using barcode information from the 10x Genomics Feature Barcoding Multiplexing kit. Filtered gene-barcode matrices were imported into R for downstream analysis with Seurat[124–126] (v5.2.1). Sample metadata, including tissue source (dura, skull, nasal) and ZsGreen status, were derived from sample identifiers and added to the object. Cells were filtered based on standard quality metrics: those with fewer than 200 detected genes, more than 6,000 genes, or over 10% mitochondrial transcript content were removed. Additional thresholds for total UMI counts and gene complexity were used to refine filtering. Doublets were identified and excluded using DoubletFinder,[127] with the expected doublet rate set to 7.5% and neighborhood size optimized per tissue. Each tissue was processed separately for normalization, feature selection, and dimensionality reduction. PCA was performed on the top variable genes, and Harmony was applied for sample-level integration within each tissue type to account for technical variation.

Clustering and cell annotation

Each tissue dataset (dura, skull, nasal) was independently preprocessed, including normalization, scaling, and principal component analysis (PCA), followed by batch correction using Harmony.[128] The top 30 PCs were used to construct a shared nearest neighbor

Please cite this article in press as: Chayama et al., Physiological brain clearance architecture revealed by neuronal protein tracing, Cell (2026), https://doi.org/10.1016/j.cell.2026.04.048

graph and perform unsupervised clustering using the Leiden algorithm, with resolution parameters adjusted (0.2–0.4) based on tissue complexity. UMAP was applied for two-dimensional visualization. Clusters were reviewed post hoc and iteratively filtered to remove low-quality or artifactual populations, including those with elevated mitochondrial content, ambiguous transcriptomic profiles, or contaminant gene signatures (e.g., skeletal muscle). Following removal, re-clustering was performed and new markers based on final objects were used for cell type annotation. In the nasal dataset, initial clustering identified neuronal clusters based on strong expression of Snap25, Rbfox3, and Tubb3. Neuronal and non-neuronal compartments were then independently subset and reprocessed to optimize subtype resolution. Cluster-specific marker genes were identified via differential expression testing. Final annotations were guided by reference to published adult mouse single-nucleus RNA-seq atlases. Annotated objects were saved for downstream tissue-specific and integrative analyses.

Differential expression analysis

To identify transcriptional differences associated with ZsGreen expression, differential expression analysis was performed using Memento[129] (v0.1.5), a model-aware framework optimized for single-cell RNA-seq count data. Analyses were conducted independently for each tissue (brain, dura, skull, and nasal) and within each annotated cell type. From each tissue-specific Seurat object, both normalized (data slot) and raw UMI count matrices (counts slot) were exported to AnnData format to preserve full expression and metadata information. For differential testing, only raw counts were used, consistent with Memento's statistical model. Within each annotated cell type, cells were filtered to include only those labeled as ZsGreen+ or ZsGreen− in the ZsGreen metadata column. A binary label was created (0 = negative, 1 = positive) for use in the model. Genes not detected in at least 10% of cells in either group were excluded. Cell types with fewer than 10 cells in both ZsGreen+ and ZsGreen− groups were skipped.

Differential expression was performed using Memento's binary_test_1d function, with a fixed capture rate of 0.25 and 5,000 bootstrap iterations. Sparse count matrices were converted to compressed sparse row (CSR) format for memory efficiency. The test produced mean expression estimates and raw p-values, which were corrected for multiple testing using the Benjamini-Hochberg procedure. Genes with adjusted p-values < 0.05 were considered significantly differentially expressed.

Monocle Trajectory and Module Analysis

Trajectory analysis was conducted using Monocle3[130–132] on skull-derived B-lineage cells to model the transition from pre-B cells to B cells. Cells were embedded using UMAP, clustered, and ordered in pseudotime, with the trajectory rooted in the Pre B cell population. Pseudotime values were transferred back to the Seurat object. To assess immune regulation along the trajectory, a tolerogenic module score was computed based on expression of *Ptpn22, Zbtb20, Cd274* genes.[97] Scores were visualized across pseudotime and compared between ZsGreen+ and - cells using statistical tests, including Wilcox.

Statistical analysis

Statistical analysis and data visualization were performed using GraphPad Prism or R. The specific statistical tests used, including corrections for multiple comparisons, are indicated in the respective figure legends. The number of biological replicates for each experiment is provided in the respective figure legends. In box plots, the horizontal bar shows the median. Error bars throughout represent standard error of the mean. Hierarchical clustering was performed in to identify clustering with the number of clusters (k) selected based on optimal silhouette score. For Gene Ontology (GO) analysis, minimum 10 or 20 group size and maximum of 3000 was used. Statistical significance is indicated in each figure legend.

Supplemental figures

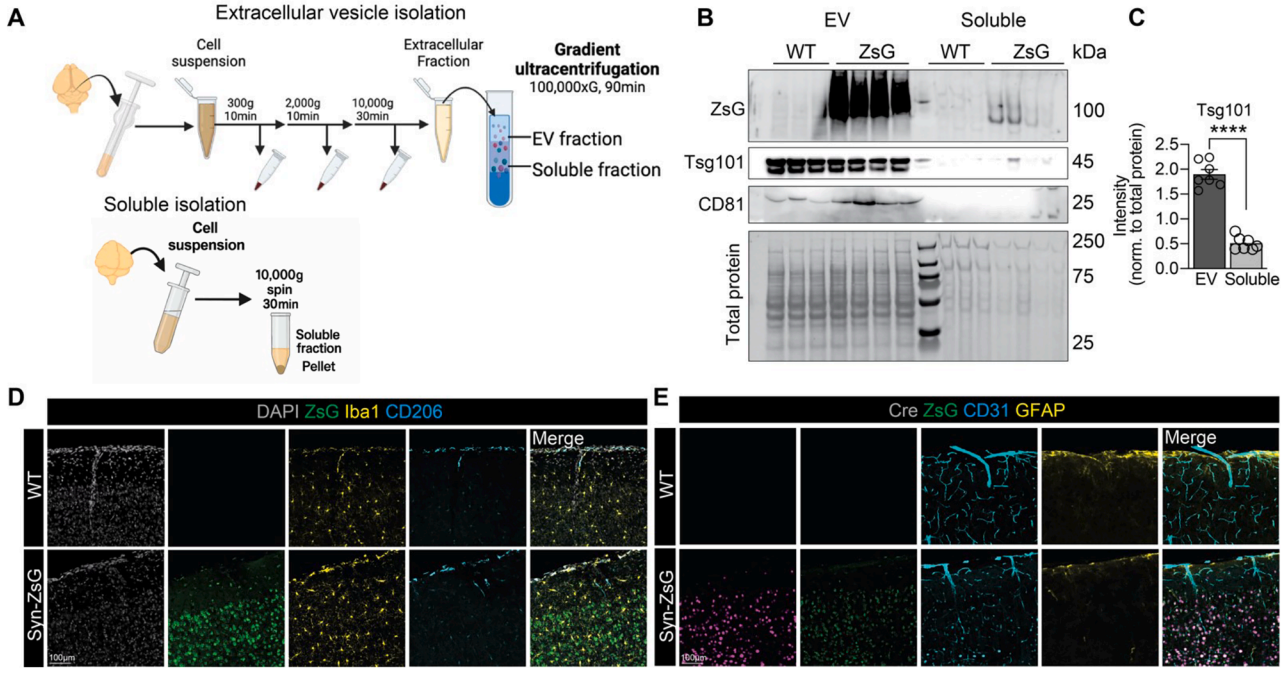

Figure S1. EV isolation paradigm and ZsGreen distribution in brain sections, related to Figure 1

(A) Schematic of biochemical strategy for EV and soluble fraction isolations from brain homogenates.

(B and C) Full WB of EV protein fractions from brain homogenates shows enrichment of EV marker Tsg101 in the EV fraction and ZsGreen detection in Syn-ZsG with no detection of ZsGreen in the WT controls. (C) Quantification of Tsg101 shows significant enrichment of EVs in the EV fraction.

(D and E) IHC analysis of brain sections from WT and Syn-ZsG mice shows DAPI, Cre, ZsG, Iba1, CD206, CD31, and GFAP staining, confirming exclusive ZsGreen and Cre expression in Syn-ZsG.

All data are mean ± SEM with $n = 3–4$. $^{*}p \leq 0.05$, $^{**}p \leq 0.01$, $^{***}p \leq 0.001$, and $^{****}p \leq 0.0001$ by Student's t test.

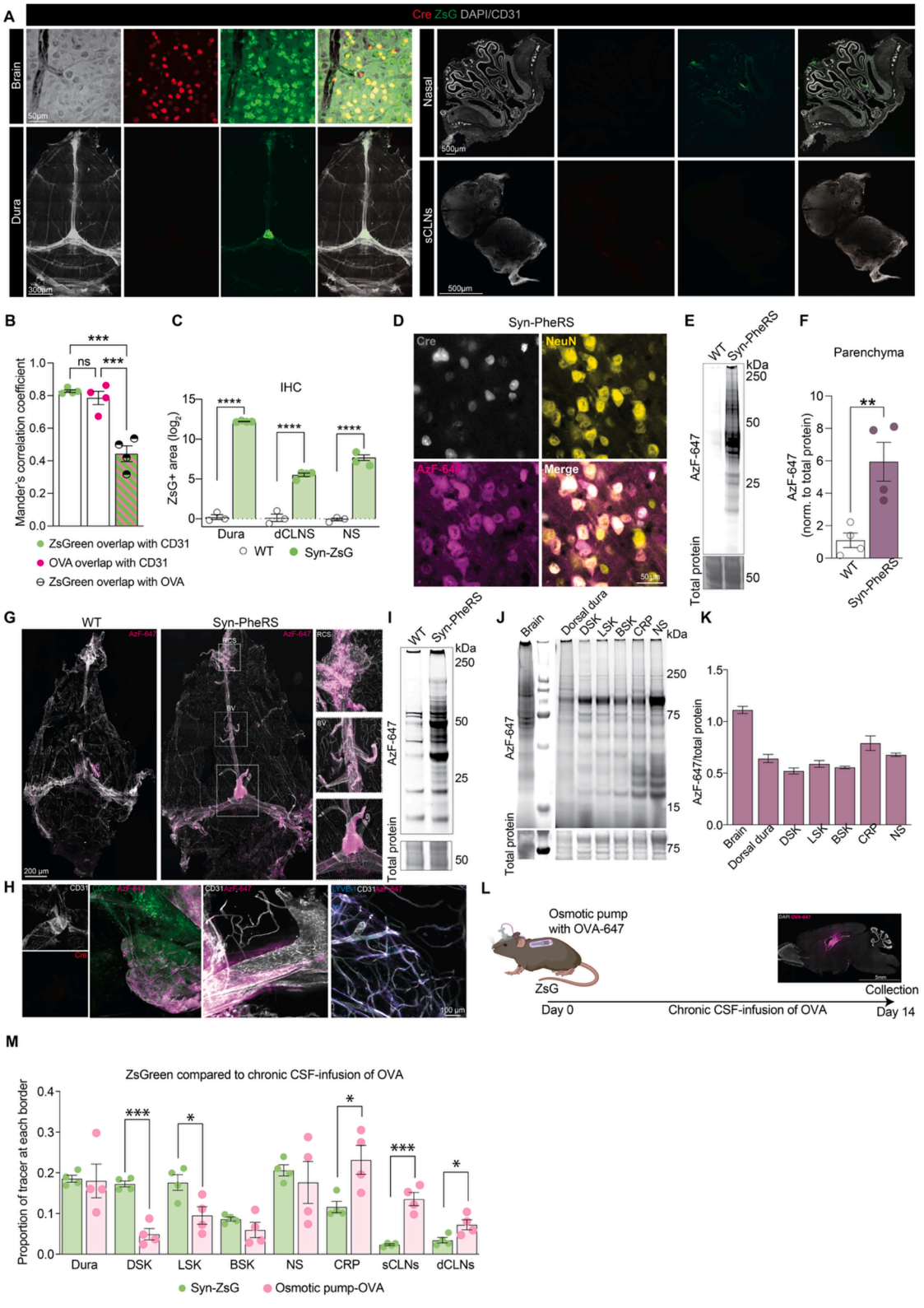

(legend on next page)

Figure S2. ZsGreen paradigm validated by tracing endogenous neuronal protein clearance, related to Figure 2

(A) IHC of brain, dura, NS, and sCLNs from Syn-ZsG mice confirms Cre-dependent ZsGreen expression restricted to neuronal compartments, with brain border tissues remaining Cre-negative.

(B) Quantification of ZsGreen and OVA-647 colocalization with $CD31^+$ vasculature in dural whole mounts using Mander's correlation coefficients. While both tracers localize perisinusally, only ~40% of the ZsGreen signal overlaps with OVA-647, indicating distinct distribution and uptake patterns.

(C) Quantification of IHC signal intensity in dura, dCLNs, and NS demonstrates significantly elevated ZsGreen abundance in Syn-ZsG mice compared with WT controls.

(D and E) Validation of the Syn-PheRS paradigm using click detection (AzF-647) of AzF-incorporated proteins in brain sections (D) and corresponding in-gel fluorescence analysis (E) of brain homogenates confirming significant labeling of Syn-PheRS brains.

(F) Quantification of AzF-647 in-gel fluorescence intensity demonstrates significantly increased AzF-labeled protein abundance in Syn-PheRS mice compared with WT controls.

(G) Dural whole mounts from WT and Syn-PheRS mice demonstrate the distribution of AzF-labeled neuronal proteins in Syn-PheRS mice paralleling anatomical patterns observed in the Syn-ZsG paradigm.

(H) High-magnification views of dural whole mounts from Syn-PheRS mice show AzF-labeled neuronal proteins colocalized with CD206, CD31, and LYVE-1.

(I) In-gel fluorescence analysis of dura homogenates confirms the presence of AzF-labeled neuronal proteins in Syn-PheRS compared with WT.

(J and K) Representative in-gel fluorescence assay and quantification of AzF-647-labeled proteins from brain border homogenates confirm the detection of endogenously produced neuronal proteins at each brain border.

(L) Experimental schematic illustrating chronic CSF infusion of OVA-647 via osmotic pump and subsequent tissue collection.

(M) Quantification comparing the proportion of ZsGreen or OVA at each border from Syn-ZsG versus chronically CSF-infused OVA-647, respectively. Plotting this data showed that chronic tracer delivery recapitulates a similar distribution observed after acute ICM injection (Figure 2D), with significantly more OVA at sCLNs and dCLNs. SS/BV, sagittal sinus/bridging veins; COS, caudal confluence of sinus; ROS, rostral confluence of sinus; TS, transverse sinus. All data are mean ± SEM with $n = 3–4$. $^*p \leq 0.05$, $^{**}p \leq 0.01$, $^{***}p \leq 0.001$, and $^{****}p \leq 0.0001$ by one-way ANOVA with Tukey's post hoc or Student's t test.

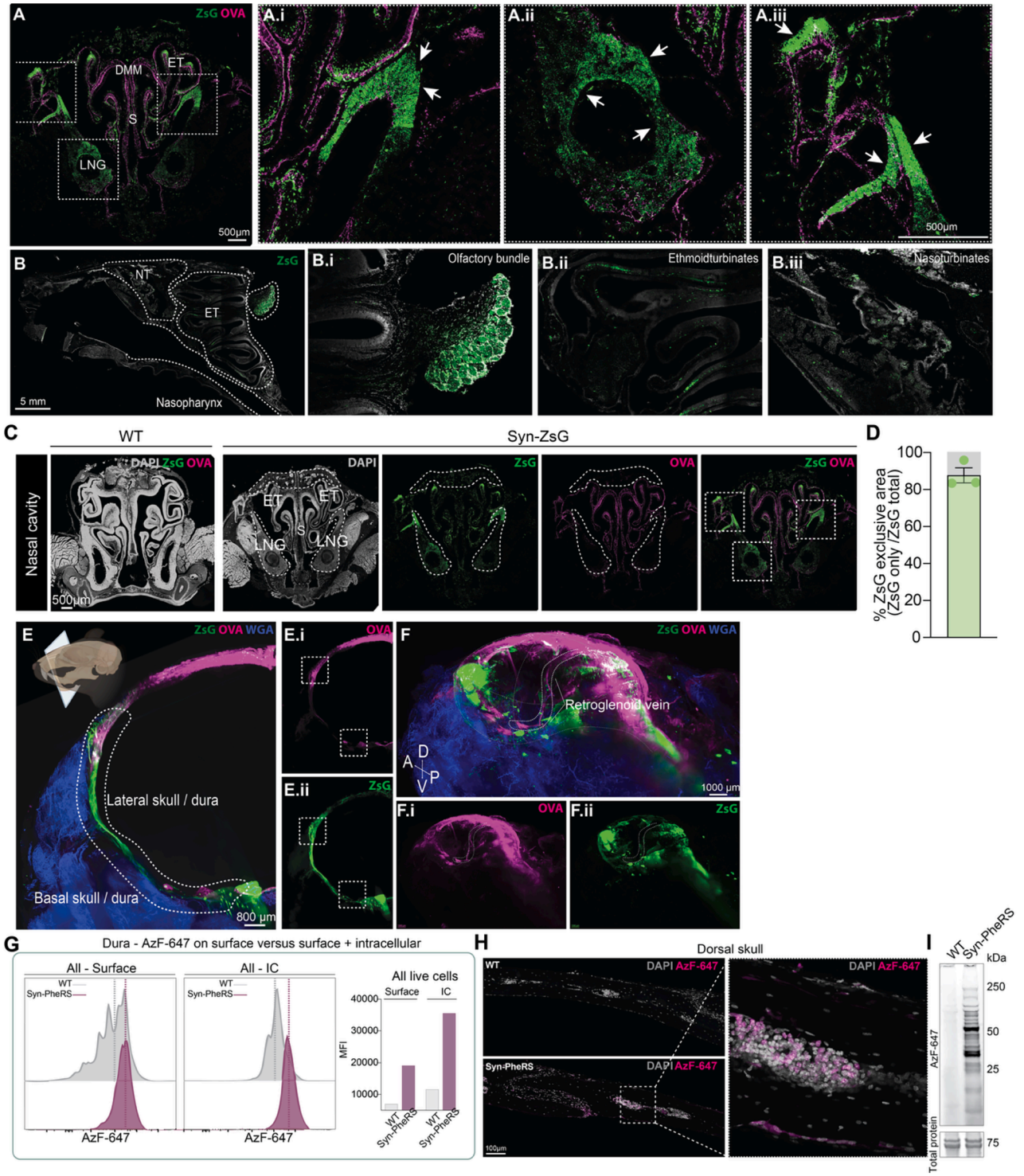

Figure S3. LSFM and IHC analyses reveal a pattern of ZsGreen and ICM-injected OVA tracer, related to Figure 3

(A–C) IHC on coronal and sagittal NS sections highlights that despite both ZsGreen and OVA-647 being detected, the signals are not concentrated in similar anatomical regions. (i–iii) Zoom in of boxed regions. DMM, dorsal medial meatus; ET, ethmoturbinates; LNG, lateral nasal gland; S, septum.

(D) Quantification of the proportion of area that is exclusively ZsGreen positive across NS sections shows that ~85% of the total ZsGreen positive area does not colocalize with OVA-647.

(legend continued on next page)

(E and F) LSFM of whole heads with the brain removed allows visualization of protein distribution across dura and skull compartments. (E) shows ZsGreen drainage along the lateral and basal dura and skull, regions with distinct spatial differences compared with OVA-555. (F) LSFM additionally highlighted the retroorbital vein.

(G) Flow cytometric analysis of all dural cell populations from WT and Syn-PheRS mice following click labeling of AzF-incorporated neuronal proteins (AzF-647). The AzF-647 signal was quantified before (surface) and after permeabilization (intracellular + surface), revealing increased intracellular accumulation of neuron-derived proteins across dural cell populations in Syn-PheRS mice compared with WT.

(H and I) Immunostaining of DSK sections and in-gel fluorescence assay from WT and Syn-PheRS mice following click detection of AzF-labeled neuronal proteins (AzF-647).

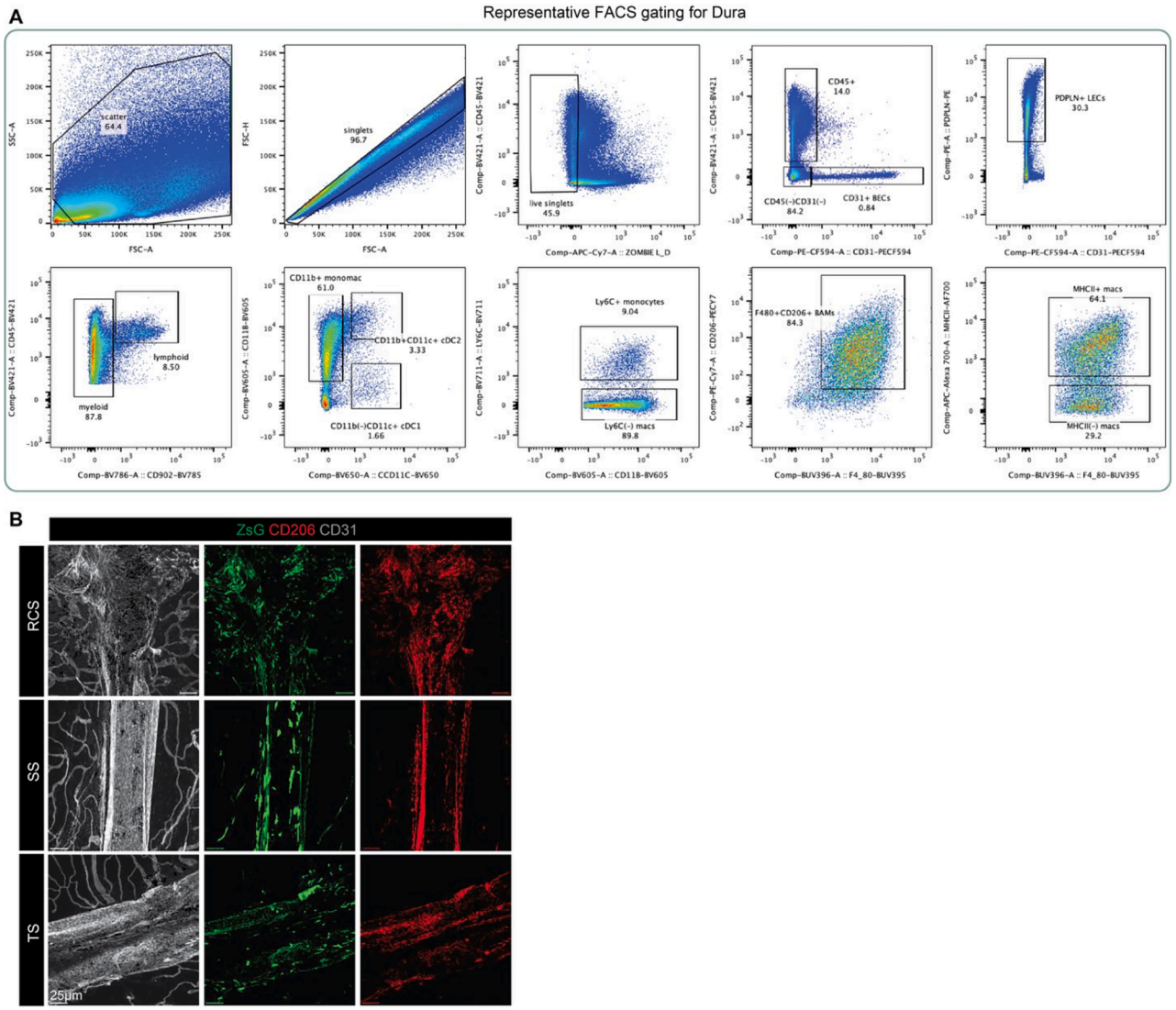

Figure S4. Representative flow cytometry gating of dural cell populations, related to Figure 4

(A) Representative flow cytometry-based gating of the cell type population in the dorsal dura. BECs: CD45(−)CD31+; LECs: CD45(−)CD31(−)PDPLN+; cDC1: CD45hiCD11b(−)CD11c+; cDC2: CD45hiCD11b+CD11c+MHCII+; CD206+ BAMs: CD45hiCD11b+CD206+; monocytes: CD45hiCD11b+Ly6C+; macs: CD45hiCD11b+F480+CD206(−).

(B) IHC of dura whole mounts from Syn-ZsG mice highlighting CD206 colocalization with ZsGreen (merges in Figure 4D). SS/BV, sagittal sinus/bridging veins; RCS, rostral confluence of sinus; and TS, transverse sinus.

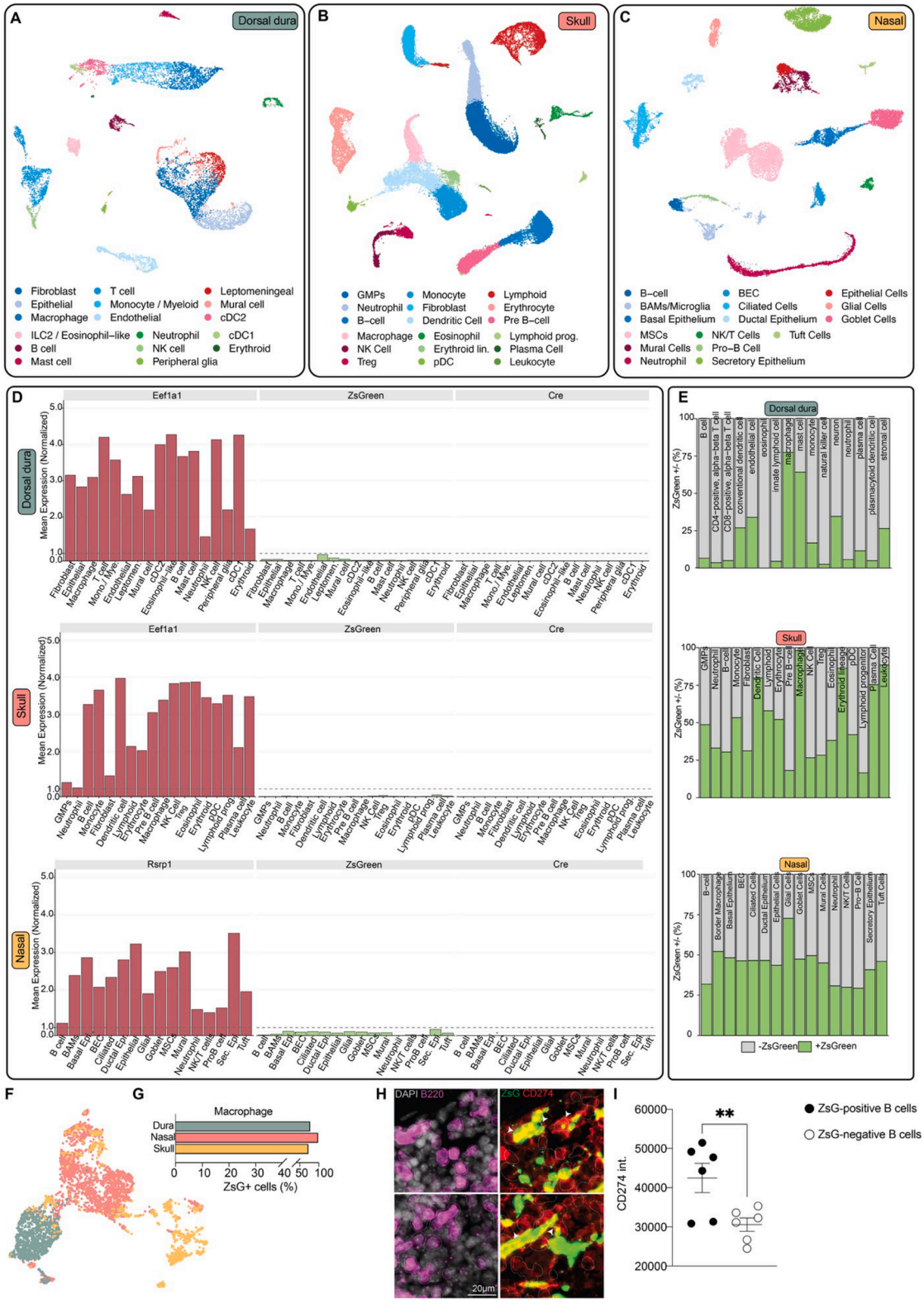

(legend on next page)

Figure S5. Flow cytometry and scRNA-seq of ZsGreen distribution across dura, skull, and nasal borders, related to Figure 4

(A–C) UMAP of cell type clusters in (B) dorsal dura, (C) DSK, and (D) NS. Cell types in each tissue are annotated by unique colors.

(D) ZsGreen and Cre transcripts are not detectable across all cell types in dorsal dura, skull, and NS compared with housekeeping genes. Mean expression for genes is plotted.

(E) Proportion of ZsGreen+ and ZsGreen− cells within each resident cell population in the dorsal dura, skull, and nasal based on scRNA-seq analysis.

(F and G) Merged UMAP of macrophage annotated cells across dorsal dura, skull, and nasal borders showing distribution of ZsGreen+ and ZsGreen− cells.

(H and I) Quantification of CD274 intensity at ZsGreen+ B cells compared with ZsGreen− B cells in DSK section. Three sections each from $n = 2$.

All data are mean ± SEM with $n = 2$–4. *$p \leq 0.05$, **$p \leq 0.01$, ***$p \leq 0.001$, and ****$p \leq 0.0001$ by Student's t test.

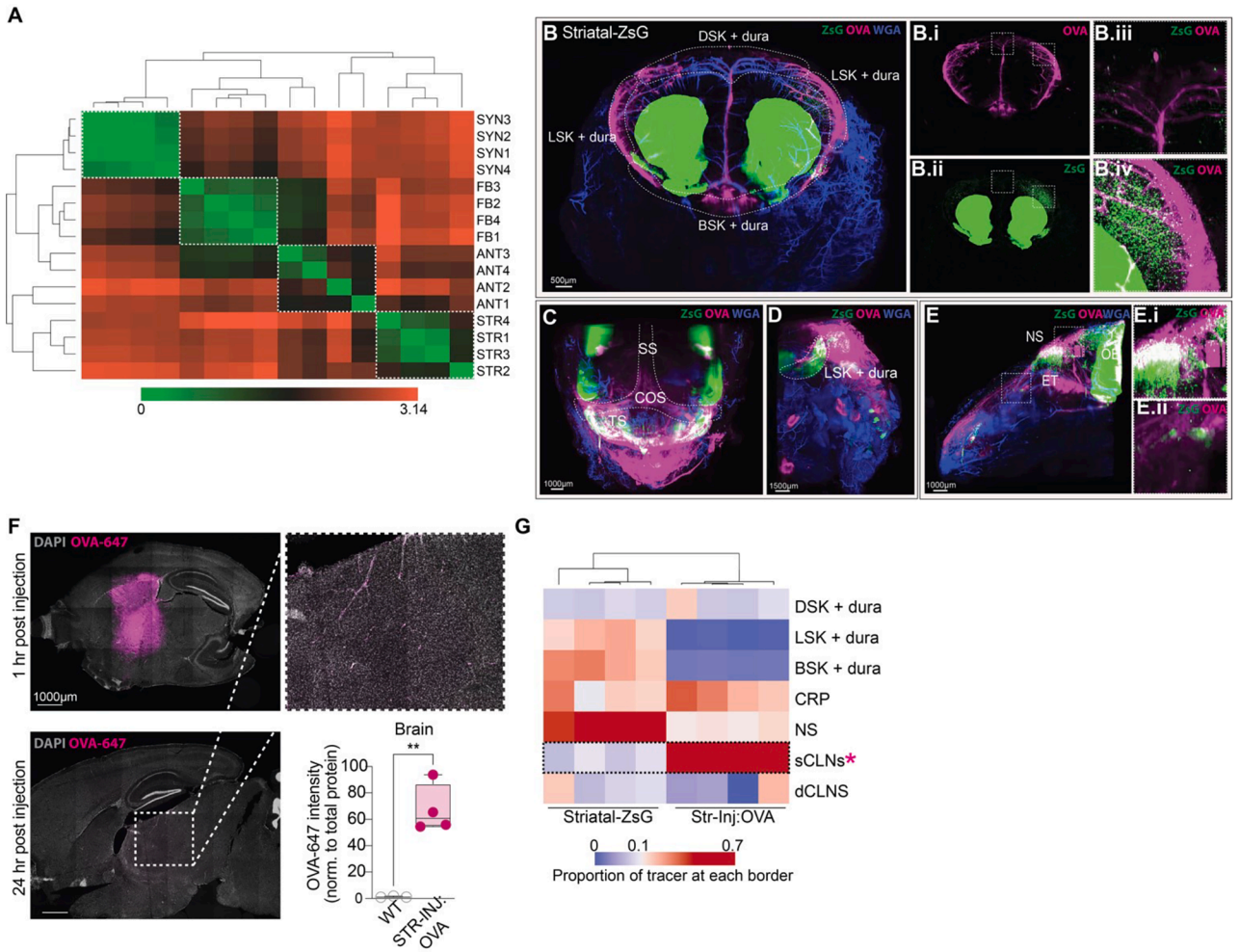

Figure S6. Brain region-specific ZsGreen labeling reveals spatially compartmentalized protein clearance and distinct routing compared with intraparenchymal tracer injection, related to Figure 5

(A) Distance matrix of normalized ZsGreen proportion across the brain border and drainage tissues comparing pan-neuronal (Syn-ZsG) and regionally restricted labeling paradigms (forebrain-ZsG, anterior-ZsG, and striatal-ZsG).

(B–E) LSFM imaging of CUBIC-cleared whole heads from striatal-ZsG mice showing ZsGreen distribution, including LSK + dura, BSK + dura, and NS.

(F) Representative IHC of brain sections following intraparenchymal injection of OVA-647 into the striatum (Str-Inj:OVA). Images show tracer localization in the striatum 1 h post-injection and substantial clearance by 24 h, confirming tracer clearance from the injection site. After 1 h, brain OVA-647 levels were quantified and compared with WT controls.

(G) Heatmap comparing the proportion of ZsGreen (Str-ZsG) versus intraparenchymal OVA-647 (Str-Inj:OVA) detected across brain borders and drainage tissues. In contrast to ZsGreen, intraparenchymal OVA shows relative underrepresentation at skull-associated borders and increased accumulation in sCLNs.

All data are mean ± SEM with $n = 3–4$. *$p \leq 0.05$, **$p \leq 0.01$, ***$p \leq 0.001$, and ****$p \leq 0.0001$ by Student's t test.

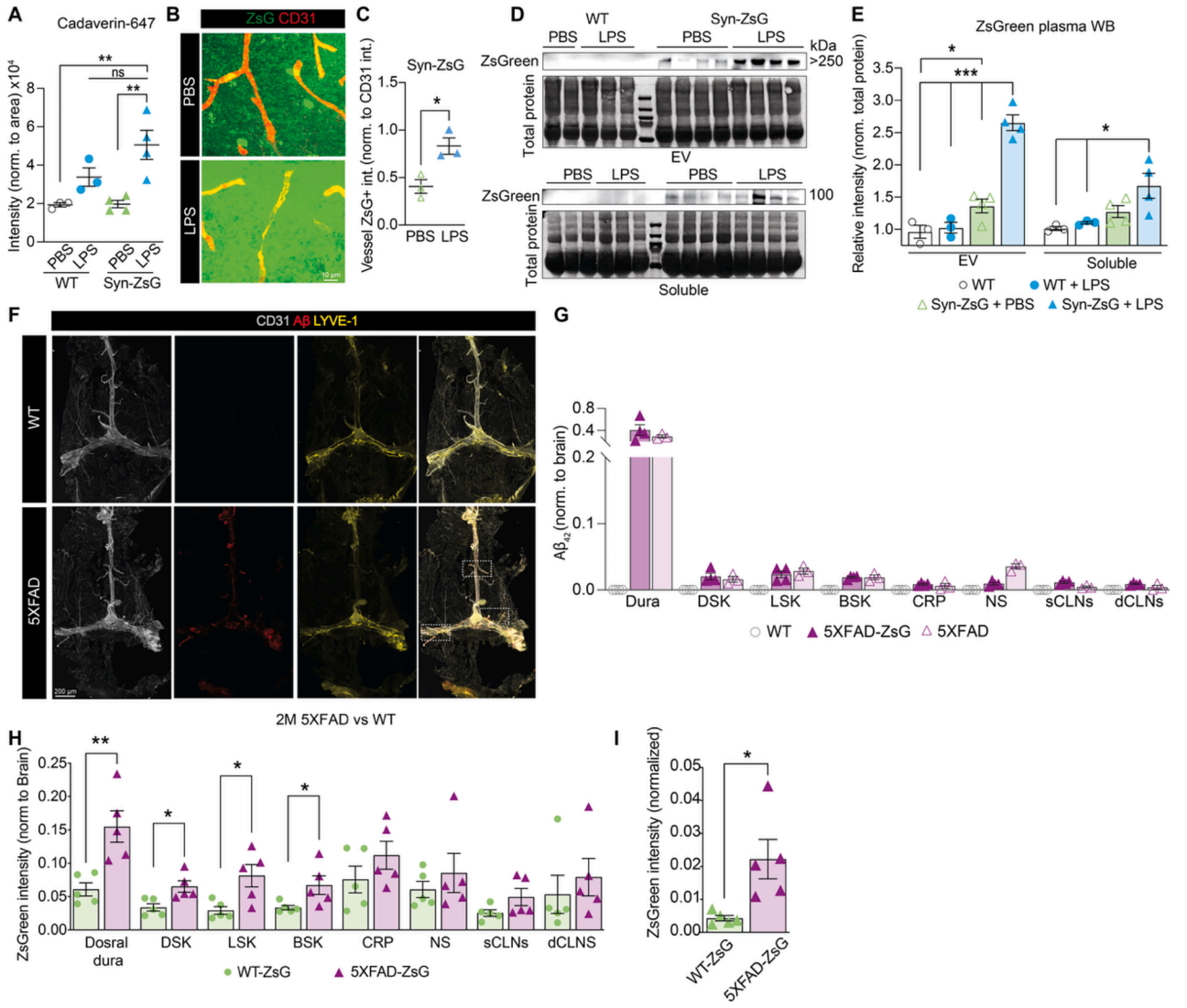

Figure S7. LPS and 5XFAD alter brain-derived protein drainage, related to Figure 6

(A) Quantification of Cadaverin-647 intensity from IHC images from Figure 6B confirms LPS-induced acute inflammation results in a compromised BBB as shown with the significantly elevated levels of the Cadaverin-647 tracer in the brain after treatment compared with controls.

(B and C) IHC analysis and quantification of brain sections from Syn-ZsG PBS- and LPS-treated mice show significantly increased abundance of ZsGreen at $CD31^+$ vessels.

(D) WB analysis of ZsGreen in plasma EV and soluble fractions shows significantly increased ZsGreen signal in LPS-treated Syn-ZsG mice compared with controls.

(E) Quantification of (C). ZsGreen from plasma EV and soluble fractions confirms significantly elevated ZsGreen levels after LPS. Total protein normalization was used for all comparisons.

(F) IHC of dura whole mounts from WT and 5XFAD mice highlights the anatomical distribution of $A\beta_{42}$. Zoom in of boxes is shown in Figure 6K.

(G) $A\beta_{42}$ ELISA from brain border extracts from WT, 5XFAD-ZsG, and 5XFAD mice confirms that ZsGreen expression does not perturb the normal drainage routing of endogenous $A\beta_{42}$.

(H) 2-month-old WT-ZsG and 5XFAD-ZsG clearance of ZsGreen across brain borders quantified by fluorescent plate reader and normalized to the respective brain's ZsGreen.

(I) ZsGreen abundance in blood plasma of 2-month-old 5XFAD mice was significantly increased compared with WT-ZsG healthy controls

All data are mean ± SEM with $n = 3–5$. $^*p \leq 0.05$, $^{**}p \leq 0.01$, $^{***}p \leq 0.001$, and $^{****}p \leq 0.0001$ by one-way ANOVA with Tukey's post hoc or Student's t test.